FEDERAL UNIVERSITY OF SANTA CATARINA (UFSC)
TECHNOLOGICAL CENTER (CTC)
GRADUATE PROGRAM IN MATERIALS SCIENCE AND ENGINEERING (PGMAT)

Mirele Horsth de Paiva Teixeira

Modelling of Fast Sintering by the Discrete Element Method: deployment, application, and validation

Florianópolis
2023

Mirele Horsth de Paiva Teixeira

Modelling of Fast Sintering by the Discrete Element Method: deployment, application, and validation

Thesis presented to the Graduate Program in Materials Science and Engineering of the Federal University of Santa Catarina as a requirement for obtaining the Degree of Doctor in Materials Science and Engineering.

Advisor: Prof. João Batista Rodrigues Neto, Dr.
Co-advisors: Prof. Dachamir Hotza, Dr.
Prof. Sergio Y. Gómez González, Dr.

Florianópolis
2023

Teixeira, Mirele Horsth de Paiva
Modelling of Fast Sintering by the Discrete Element Method: deployment, application, and validation / Mirele Horsth de Paiva Teixeira ; orientador, João Batista Rodrigues Neto, coorientador, Dachamir Hotza, coorientador, Sergio Yesid Gómez González, 2023.
96 p.

Tese (doutorado) - Universidade Federal de Santa Catarina, Centro Tecnológico, Programa de Pós-Graduação em Ciência e Engenharia de Materiais, Florianópolis, 2023.

Inclui referências.

1. Ciência e Engenharia de Materiais. 2. Sinterização Rápida. 3. Simulação Numérica. 4. Microestrutura. 5. Gradientes Térmicos. I. Rodrigues Neto, João Batista . II. Hotza, Dachamir. III. González, Sergio Yesid Gómez IV. Universidade Federal de Santa Catarina. Programa de Pós-Graduação em Ciência e Engenharia de Materiais. V. Título.

Mirele Horsth de Paiva Teixeira

Modelling of Fast Sintering by the Discrete Element Method: deployment, application, and validation

This thesis was presented to obtain the title of Ph.D. and approved on September 4th, 2023, by the examination board composed of the following members:

Prof. Dereck Nills Ferreira Muche, Dr.
UFSCar

Prof. Agenor De Noni Jr., Dr.
UFSC

Prof. Bruno Alexandre Pacheco de Castro Henriques, Dr.
UFSC

We certify that this is the original and final version of the complete work considered adequate to obtain the Ph.D. in Materials Science and Engineering.

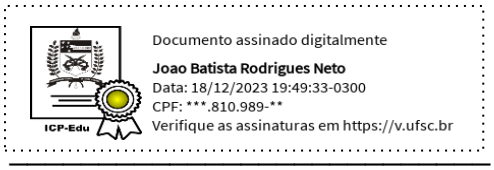

Prof. João Batista Rodrigues Neto, Dr.
PGMAT-UFSC Coordinator

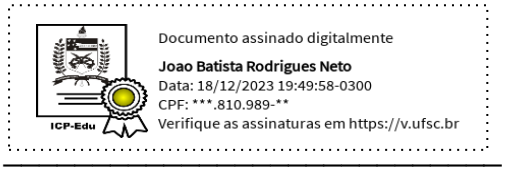

Prof. João Batista Rodrigues Neto, Dr.
Advisor

Florianópolis, 2023.

ACKNOWLEDGEMENTS

To God, who gives me the energy of life every day, gives me strength and courage to achieve my goals, and is my help in times of distress.

To my parents, Rachel and Anselmo (*in memoriam*), who taught me the value of education from a very early age and that there are no limits to our dreams.

To my fiancé Julio Cesar for his support during this journey. Even a continent away, it has always offered a safe harbor in the many storms on this journey.

To Professors Dachamir Hotza, João Batista R. Neto, Agenor De Noni, and Sergio Y. Gómez González for seeing my potential and offering me challenges that boosted my personal and professional skills. Also, thank you for the confidence placed in my project proposal.

Special thanks to Dr. Maksym Dosta, M.Sc. Vasyl Skorych, Dr. Rolf Janssen (*in memoriam*), and Prof. Dr. Stefan Heinrich for the warm welcome at the Hamburg University of Technology and guidance during my sandwich PhD period.

To the SPE 2019-2020 team for providing me with a pleasant cultural adaptation process in Hamburg and sharing great times.

To UFSC and TUHH for the infrastructure and opportunity to develop the research.

To Rogério Antônio Campos for the efficiency with which he performs his work in front of the PGMAT/UFSC secretariat, friendliness, and willingness to help students.

To CNPq, CAPES, DFG, and DAAD for funding during this period.

To my friends in general for their support and friendship over all these years. Last but not least, I thank all those who contributed, directly or indirectly, to completing the Ph.D. degree.

AGRADECIMENTOS

A Deus, que me presenteia todos os dias com a energia da vida, me proporciona força e coragem para atingir meus objetivos e é meu socorro nas horas de angústias.

Aos meus pais Rachel e Anselmo (*in memoriam*) que desde muito cedo me ensinaram o valor da educação e que me mostraram que não há limites para nossos sonhos.

Ao meu noivo Julio Cesar, pelo apoio durante essa caminhada. Mesmo a um continente de distância, sempre ofereceu um porto seguro nas muitas tempestades enfrentadas nessa jornada.

Aos Professores Dachamir Hotza, João Batista R. Neto, Agenor De Noni e Sergio Y. Gómez González, por enxergarem o meu potencial, me proporem desafios que impulsionaram meu desenvolvimento pessoal e professional. Também, pela confiança depositada na minha proposta de projeto.

Agradecimento especial ao Dr. Maksym Dosta, M.Sc. Vasyl Skorych, Dr. Rolf Janssen (*in memoriam*) e Prof. Dr. Stefan Heinrich pela calorosa recepção na Universidade de Tecnologia de Hamburgo e orientação durante meu período de doutorado sanduíche.

A toda a equipe SPE 2019-2020, por me acolherem, ensinarem e proporcionarem um processo de adaptação cultural agradável e por todos os momentos de descontração que compartilhamos.

À UFSC e TUHH pela infraestrutura e oportunidade de desenvolver a pesquisa.

Ao Rogério Antônio Campos pela eficiência com a qual desempenha seu trabalho frente a secretaria do PGMAT/UFSC, pela simpatia e disposição em auxiliar os alunos.

Ao CNPq, CAPES, DFG e DAAD pelo financiamento durante este período.

Aos meus amigos em geral, pelo apoio e amizade ao longo de todos esses anos. Por último e não menos importante, a todos aqueles que contribuíram, de maneira direta ou indireta, para o êxito na conclusão do doutorado.

“I never loose. Either I win, or I learn”

Nelson Mandela

"Science never solves a problem without creating at least ten more”

George Bernard Shaw

ABSTRACT

The present work aimed to develop an original numerical model to reveal the thermo-micro-mechanical behavior of particulate systems and their densification process under sintering at high heating rates. The model was built by extending the numerical sintering model and coupling it with thermomechanical concepts. The model was developed using the discrete element method in the MUSEN software. The formulation elaborated here was applied to the rapid sintering of Al_2O_3 and validated with experimental data from the literature. Emphasis was given to the evolution of thermal and densification gradients along sample length and as a function of sintering parameters such as the heating rate and temperature. The model predicted the microstructure formation, shrinkage, and progress of the densification front. The relationships between internal defects, microstructure, sintering temperature, and heating rate were further analyzed. Compared with experimental data from the literature, the numerical results showed good agreement, denoted by $r^2 = 0.98$ and Pearson's $r = 0.99$. Finally, the evolution of the microstructure throughout the process concerning the coordination number, normalized contact radius distribution, and temperature gradients along the length of the sample were explored.

Keywords: Fast Sintering; Numerical Simulation; Discrete Element Method; Microstructure; Thermal Gradients; Defect Evolution.

RESUMO

O presente trabalho teve como objetivo desenvolver um modelo numérico original para revelar o comportamento termomicromecânico de sistemas particulados e seu processo de densificação sob sinterização em altas taxas de aquecimento. O modelo foi construído estendendo o modelo numérico de sinterização e acoplando-o a conceitos termomecânicos. O modelo foi desenvolvido pelo método dos elementos discretos, no software MUSEN. A formulação aqui elaborada foi aplicada na sinterização rápida de Al_2O_3 e validada com dados experimentais da literatura. Foi dada ênfase à evolução dos gradientes térmicos e de densificação ao longo do comprimento da amostra e em função dos parâmetros taxa de aquecimento e temperatura de sinterização. A formação da microestrutura, retração e o progresso da frente de sinterização foram previstos pelo modelo. As relações entre defeitos internos, microestrutura, temperatura de sinterização e taxa de aquecimento foram posteriormente analisadas. Comparados com dados experimentais da literatura, os resultados numéricos apresentaram boa concordância, denotada pelo $r^2 = 0,98$ e Pearson's $r = 0,99$. For fim, a evolução da microestrutura através ao longo do processo em relação ao número de coordenação, distribuição do raio de contato normalizado, gradientes de temperatura ao longo do comprimento da amostra foram explorados.

Palavras-chave: Sinterização Rápida; Simulação Numérica; Método dos Elementos Discretos; Microestrutura; Gradientes Térmicos; Evolução de Defeitos.

RESUMO EXPANDIDO

MODELAGEM DA SINTERIZAÇÃO RÁPIDA PELO MÉTODO DOS ELEMENTOS DISCRETOS: DESENVOLVIMENTO, APLICAÇÃO E VALIDAÇÃO

Introdução

A sinterização é uma etapa crítica na evolução microestrutural dos componentes produzidos pela tecnologia do pó, na qual materiais, inicialmente particulados, são transformados em um corpo com maior densidade. Apesar do contínuo desenvolvimento teórico desde o final da década de 1940, e, dos notáveis avanços das técnicas analíticas, ainda há espaço para melhorias na compreensão dos fenômenos de rearranjo, densificação e transferência de calor em sistemas particulados sob sinterização rápida.

No contexto de digitalização da indústria e desenvolvimento de materiais e processos, abordagens numéricas incluindo o método dos elementos finitos (do inglês *Finite Element Method* - FEM), o método dos volumes finitos (do inglês *Finite Volume Method* - FVM) e o método dos elementos discretos (do inglês *Discrete Element Method* - DEM), têm ganhado notoriedade.

Os métodos acima citados, especialmente o DEM e o FEM, têm sido aplicados extensivamente para modelar interações interpartículas durante a sinterização convencional, ou seja, considerando baixas taxas de aquecimento tal que a temperatura experimentada pelo corpo em sinterização é constante. No entanto, abordagens de sinterização sob altas taxas de aquecimento, que incluem condições temperatura transiente durante o processo, ainda são escassas e apresentam suposições irrealistas, como considerar um corpo cerâmico à verde como um sólido não poroso e a ausência de retração.

O DEM, especificamente, é um método que permite a avaliação do comportamento individual das partículas pertencentes ao arranjo ou corpo de prova, o que é crucial para desvendar o comportamento em microescala durante o processo de sinterização. No presente trabalho, a formulação de sinterização de Parhami &

McMeeking foi estendida para incluir regime não estacionário de temperatura durante o processo de sinterização rápida, a fim de preencher as lacunas de evolução em microescala da sinterização em condições não isotérmicas, como a sinterização rápida.

Objetivos

O presente trabalho tem como objetivo principal desenvolver e implementar um modelo numérico original a partir da expansão modelo de sinterização de Parhami & McMeeking para condições não-isotérmicas e acoplamento de fenômenos termomecânicos visando avaliar o comportamento termo-micro-mecânico de sistemas particulados sob sinterização rápida, através do DEM.

Dentro desse escopo, os objetivos específicos incluem:

- Aplicação e validação do modelo a um sistema cerâmico;
- Investigação da evolução dos gradientes térmicos e de densificação durante a sinterização;
- Análise da evolução da microestrutura, retração e fenômenos característicos de densificação;
- Avaliação de relações entre defeitos, microestrutura e parâmetros de sinterização.
- Investigação das microevoluções de microestrutura dependentes do tempo relativas ao número de coordenação e à distribuição do raio de contato interpartícula.

Metodologia

- **Constituição do corpo de prova virtual**

A amostra numérica foi criada a fim de manter o máximo de semelhança com a amostra experimental, produzida por García e colaborados (2011). Portanto, a amostra numérica foi gerada alocando aleatoriamente partículas esféricas com diâmetro de 0,2 μm em um volume cilíndrico. Foi implementada uma densidade relativa inicial de 0,62, e, em seguida, características físico-químicas e mecânicas da Al_2O_3 foram atribuídas as partículas recém-criadas. Devido às limitações computacionais do DEM, optou-se por preservar o tamanho das partículas e a densidade relativa inicial em detrimento das dimensões do corpo de prova de Al_2O_3. Dessa forma, o corpo de prova simulado foi construído com dimensões (diâmetro e altura) 10^3 menor que o experimental (2 cm x 2 cm), contendo aproximadamente 1,2 milhões de partículas.

- **Construção do modelo**

A abordagem termomecânica acoplada ao modelo de sinterização foi formulada para simular os gradientes térmicos tipicamente presentes durante a sinterização rápida.

As partículas foram agrupadas em duas zonas, conforme ilustrado na Figura RE1, onde as partículas cinzas pertencem a zona interna e as partículas roxas pertencem à camada externa. Com base em sua posição, as partículas foram submetidas a diferentes mecanismos de transferência de calor:

- Radiação – emitida pela vizinhança, que corresponde ao ambiente do forno, e absorvida pelas partículas externas pertencentes a superfície da amostra (ilustrada em roxo na Figura RE1);
- Convecção – entre o ar estagnado dentro do forno e as partículas na superfície da amostra (ilustrada em roxo na Figura RE1); e
- Condução – transferência de calor através de todo e qualquer contato interpartícula, sejam as partículas pertencentes a camada externa e/ou interna (ilustrada em roxo e em cinza na Figura RE1).

Figura RE1: Ilustração das camadas de partículas externas (*outer layer*) e internas (*inner layer*) e os respectivos mecanismos de transferência de calor (radiação, convecção e condução).

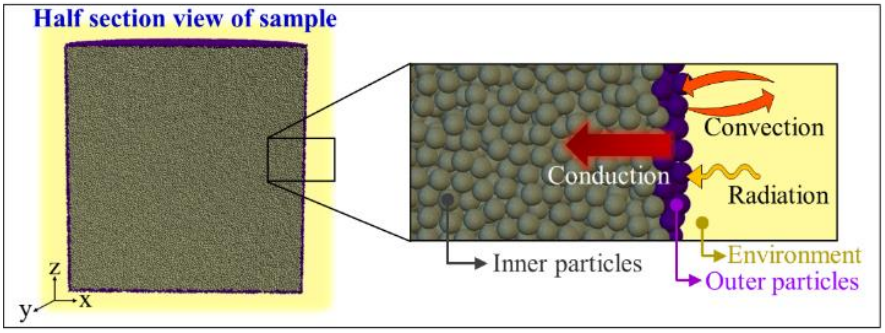

Diferentes modelos de forças de contato foram aplicados para modelar as interações termomecânicas partícula-partícula a depender de 2 critérios: temperatura média do contato interpartícula e do raio do contacto normalizado pelo raio da partícula (r_c/R).

Dados da literatura indicaram que compactados de Al_2O_3 com ~0,2 µm de diâmetro não mostraram mudanças dimensionais significativas até 1050 ºC, o que se interpretou como inatividade dos mecanismos de até esta temperatura. Portanto, essa temperatura foi implementada como critério de início da sinterização, sendo a temperatura de corte abaixo da qual não ocorre sinterização. Além disso, simulações exploratórias confirmaram que uma estrutura de empacotamento denso foi alcançada quando o raio de contato (r_c) atinge 80% do raio R das partículas primárias, ou seja, $r_c/R=0,8$. Desta forma, $r_c/R=0,8$ foi implementado como critério de parada do modelo de sinterização. Vale ressaltar que r_c/R é um parâmetro de densificação em microescala que independe do tipo de material e tamanho da amostra numérica.

Assim os modelos de força de contato aqui aplicados foram:

- Hertz-Mindlin modificado: ativado enquanto a temperatura mínima do contato interpartícula estiver inferior ou igual a 1050 ºC;
- Sinterização não isotérmica: ativado quando a temperatura mínima do contato interpartícula for superior a 1050 ºC e o r_c/R é menor ou igual a 0,8;

- Contato de força repulsiva: aplicada quando o r_c/R atinge 0,8, e, é utilizado com critério de parada a fim de evitar densificações não realísticas.

O modelo numérico foi implementado no software de código aberto MUSEN, desenvolvido no Instituto de Engenharia de Processos Sólidos e Tecnologia de Partícula da Universidade de Tecnologia de Hamburgo (SPE-TUHH).

- Condições de sinterização aplicadas no modelo

As amostras virtuais foram aquecidas da temperatura ambiente até 1050, 1250, e 1350 °C. Uma taxa de aquecimento nominal instantânea foi aplicada para se assemelhar à introdução direta da amostra em um forno à temperatura de sinterização, como descrito na metodologia experimental de García et al., 2011. Para fins comparativos e de exploração das potencialidades do modelo, taxas de aquecimento de 250 ºC/s e 10 ºC/min também foram avaliadas. O forno foi modelado apenas pelas condições de contorno aplicadas à superfície do corpo. Sua temperatura foi assumida como constante ao longo do processo, e as perdas de calor entre a amostra e o ambiente externo foram desprezadas.

Resultados e Discussão

O perfil de evolução da temperatura no corpo de prova simulado, desde a temperatura ambiente até 1050 ºC ao longo do tempo de imersão, foi analisado. As partículas externas atingiram a temperatura do forno quase imediatamente – menos de 10 s – devido à alta entrada de calor por radiação e convecção. Observou-se que inicialmente o calor tendeu a se acumular perto da superfície externa. Assim, a temperatura nesta região aumentou rapidamente enquanto as camadas mais internas de partículas permaneceram essencialmente à temperatura ambiente. Com o passar do tempo de exposição à temperatura, o núcleo da amostra numérica atingiu 48% da temperatura do forno em 60 s, e, 90% em 240 s. Em 540 s – menos de 10 min – toda a amostra numérica já havia atingido à temperatura do forno, e, o regime permanente de calor foi alcançado.

Os dados experimentais e simulados da variação de temperatura em função do tempo de aquecimento foram analisados. Uma forte correlação e ajuste foram observados. Foi obtido um R de Pearson de 0,994, expressando um notável grau de correlação linear. Além disso, 98,7% da variação no resultado da simulação foi explicada pela equação de regressão, demonstrando um bom ajuste. A concordância consistente dos resultados numérico e experimental reforça que os parâmetros do modelo térmico foram adequadamente aproximados. Os coeficientes estatísticos demonstram o potencial do modelo TMS na descrição de fenômenos térmicos nas condições de processo avaliadas.

O efeito da temperatura (1025, 1250 e 1350ºC) na cinética da sinterização foi analisado nas amostras simuladas, o que indicou que o aumento da temperatura de sinterização aumenta a densificação do corpo ao potencializar o processo de difusão mássica e térmica. O progresso da densificação implica num aumento na difusividade térmica local levando a um efeito sinérgico na taxa de aquecimento. O aumento na difusividade térmica devido à densificação proporciona um aumento substancial na velocidade de propagação do calor; portanto, os gradientes térmicos tendem a desaparecer mais cedo.

Detalhes microcinéticos acessados numericamente forneceram informações adicionais sobre o desenvolvimento microestrutural durante a sinterização rápida. Os resultados mostraram que a evolução do número de coordenação (ACN) e do raio de contato normalizado rc/R não foram homogêneos ao longo do comprimento radial do corpo de simulação. De fato, o aumento de ambos se deu da superfície externa para o centro da amostra simulada, o que pode ser atribuído aos gradientes térmicos sob condições não isotérmicas de queima rápida. Os aumentos acentuados de ACN e rc/R nas zonas mais próximas da superfície externa sugerem a formação de uma frente de densificação que tende a avançar na direção do gradiente térmico, ou seja, em direção ao interior compacto, controlando o fluxo de calor.

As dependências micro-macro foram aqui analisadas para simulação da queima rápida à 1250 e 1350 ºC. Comparativamente, uma tendência a um aumento acentuado na taxa de densificação foi registrada nos primeiros 350 s para ambas as temperaturas de sinterização. O incremento de 100 ºC na temperatura de sinterização (T_{sint} = 1350 ºC) intensificou o fluxo de calor entre as partículas levando a um aumento de quase 61% na taxa de densificação. Posteriormente, a taxa de densificação diminuiu para a amostra sinterizada a 1350 ºC, mantendo-se praticamente constante até o final do tratamento a 1250 ºC. No ponto final (1200 s), a diferença entre as taxas de densificação da sinterização a 1350 e 1250 ºC foi de apenas 13%. O progresso do raio de contato normalizado r_c/R de todas as partículas do corpo de prova em relação à temperatura de sinterização ao longo do tempo de processo revelou que a amostra queimada a 1250 ºC permaneceu sob gradiente térmico por mais 100 s. Assim, o aumento da temperatura de sinterização potencializou a taxa de densificação e a velocidade na qual os gradientes de temperatura passam por toda a amostra.

Os resultados da simulação também previram a formação da microestrutura característica devido à formação de uma frente de densificação no estágio intermediário de queima rápida: uma camada externa mais densa de partículas foi formada e envolveu a região interna porosa. A frente de densificação é o produto dos gradientes térmicos gerados pela rápida entrada de calor e é apontada como o agente controlador do fluxo de calor dentro do compacto. Assim, formar uma camada densa de Al_2O_3 na interface entre o ambiente do forno e a amostra verde tem um efeito significativo na distribuição do perfil de temperatura. Esse resultado sugere que as

altas taxas de densificação observadas durante a sinterização rápida estão relacionadas a uma alteração na estrutura interna da amostra, o que não é considerado um mecanismo de sinterização complementar, mas pode contribuir para a potencialização da sinterização.

A avaliação da retração radial das amostras de simulação sinterizadas a 1250 e 1350 ºC mostra uma retração de 10% acompanhada do incremento na densidade após 250 s de queima rápida a 1350 ºC, enquanto este valor é 2,2 vezes menor para sinterização a 1250 ºC. Aos 350 s, a retração radial progrediu para 13,6% e 7,8% para sinterização rápida a 1350 e 1250 ºC, respectivamente. Após 1200 s, o modelo TMS previu 15,4% de retração radial para o corpo de Al_2O_3 queimado rapidamente a 1350 ºC e 14,5% para sinterização a 1250 ºC. Os valores preditos para a retração radial concordam com as características de densificação em micro-macro escalas discutidas anteriormente. Além disso, os valores de retração previstos pelo presente método concordam com trabalhos experimentais anteriores.

Pequenos defeitos foram introduzidos artificialmente por deleção de partículas dentro da amostra simulada de Al_2O_3, com o objetivo de analisar o desenvolvimento da microestrutura ao redor dos defeitos. A evolução dos defeitos nas microestruturas finais após a sinterização a 1350 ºC sob 3 diferentes taxas de aquecimento - instantânea, 250 ºC/s e 10 ºC/min - em contraste com a queima rápida a 1250 ºC foi avaliada. Observou-se que a morfologia dos defeitos não apresentou dissimilaridade considerável entre altas taxas de aquecimento instantâneas e 250 ºC/s para queima rápida a 1350 ºC. No entanto, observou-se uma considerável evolução microestrutural com tendência ao fechamento de defeitos internos com a aplicação de um protocolo de queima convencional ($\check{R}$ = 10 ºC/min) a 1350 ºC. Diminuindo a temperatura de sinterização em 100ºC (T_{sint} = 1250 ºC) e mantendo a taxa de aquecimento instantânea, observou-se uma redução substancial no tamanho dos defeitos, o que levou a uma variação morfológica significativa nos defeitos com tendência à obtenção de uma microestrutura mais densa. O efeito antagônico das temperaturas e taxas de aquecimento na evolução significativa dos defeitos sob queima rápida pode ter origem, entre outros fatores, na rápida propagação do calor devido aos altos gradientes térmicos, ou seja, a propagação abrupta do calor não forneceu tempo

suficiente para ativação de mecanismos específicos que poderiam ter favorecido a transferência de massa e o alívio de tensões aprisionadas na região dos defeitos.

Considerações Finais

Neste trabalho foi desenvolvido e implementado um modelo numérico capaz de prever características que ocorrem durante a sinterização rápida, através do Método dos Elementos Discretos. O modelo foi construído unindo conceitos de transferência de calor, regimes transitórios de temperatura e forças de interação interpartícula, com objetivo simular fenômenos em micro e macro escala que ocorrem durante a sinterização à elevadas taxas de aquecimento.

Através da aplicação do modelo a um sistema cerâmico de Al_2O_3, foram obtidos detalhes dos perfis de gradientes de temperatura e de densidade. A evolução da microcinética estrutural no corpo de prova cerâmico simulado também foi acessado pelo modelo, inclusive na presença de pequenos defeitos internos. O coeficiente de determinação r^2=0,99 ressalta a confiabilidade e precisão dessa abordagem na janela de processamento analisada.

A partir da aplicação e exploração das funcionalidades do modelo DEM desenvolvido, conclui-se que ele emerge como uma ferramenta em potencial para analisar e prever fenômenos termomecânicos durante processos de sinterização rápida. Ao acessar detalhes em microescala do processo de densificação e seus mecanismos subjacentes, o modelo desenvolvido abre novos caminhos para maior exploração e otimização neste campo de estudo.

Palavras-chave: Sinterização Rápida; Simulação Numérica; Método dos Elementos Discretos; Microestrutura; Gradientes Térmicos; Evolução de Defeitos.

LIST OF FIGURES

LIST OF TABLES

TABLE OF CONTENT

CHAPTER 1 – THESIS STRUCTURE, INTRODUCTION AND OBJECTIVES

1.1 THESIS STRUCTURE

This thesis is structured in five chapters.

- Chapters 1 and 2 comprise the introduction and literature review of relevant topics related to this work.
- Chapters 3 and 4 present the research outputs. Each is divided into sections: introduction, development, results and discussion, conclusion, and references.
- Finally, in Chapter 5, the general conclusions and an outlook for future works are presented.

1.2 INTRODUCTION

Sintering is a critical step in the microstructural evolution of components produced by powder technology, in which particulate materials are consolidated to a continuous body with higher density (RAHAMAN, 2003). Despite the continuously development on sintering theory since 1940s (GERMAN, 2010), and notable advances in analytical techniques, there is still room for improvement in comprehensively understanding the rearrangement, densification, and heat transfer phenomena on particulate systems under fast sintering.

In the context of digitalization of industry and development of materials and processes, numerical approaches including the finite element method (FEM), finite volume method (FVM), and discrete element method (DEM), have been used for the modelling of thermal phenomena in fluidized and packed beds (ANDERSON et al., 2015; CHEN et al., 2019; FENG; HAN; OWEN, 2009; HADDAD et al., 2021; HADDAD; GUESSASMA; FORTIN, 2014; KIANI-OSHTORJANI; JALALI, 2019; MOSCARDINI et al., 2018; ROUSSEAU et al., 2014; SANGRÓS; SCHILDE; KWADE, 2016; TERREROS; IORDANOFF; CHARLES, 2013; VARGAS; MCCARTHY, 2002; WANG et al., 2020; WU et al., 2017; ZHOU; ZHANG; ZHENG, 2012).

The methods mentioned above, especially DEM and FEM, have been extensively applied to model interparticle interactions during conventional sintering, that is, considering low heating rates such that the temperature experienced by the sintering body is constant (BESLER et al., 2015, 2016; DOSTA et al., 2020; JAUFFRÈS et al., 2012; RASP et al., 2017; RASP; KRAFT; RIEDEL, 2013). However, sintering approaches under high heating rates, which include transient temperature conditions during the process, are still scarce and present unrealistic assumptions, such as considering a green ceramic body as a non-porous solid and the absence of shrinkage (GANERIWALA; ZOHDI, 2016; MORI, 2006).

DEM, specifically, is a method that allows the evaluation of the individual behavior of particles belonging to the arrangement or specimen, which is crucial for unveiling microscale behavior during the sintering process. In the present work, the sintering formulation of Parhami & McMeeking (PARHAMI; MCMEEKING, 1998) was extended to include non-stationary temperature regime during the rapid sintering process, in order to fill the gaps of micro-scale evolution of sintering under non-isothermal conditions, such as fast firing.

1.3 RESEARCH OBJECTIVES

The main objective of this work is to develop and deploy an original discrete element formulation for coupling thermo-mechanics with sintering, aiming to assess particulate systems' thermo-micromechanical behavior under rapid sintering.

Within this scope, specific objectives include:

- To apply and validate the model to a ceramic system by comparing simulations and experimental results;
- To investigate the evolution of thermal and densification gradients during sintering;
- To analyze the microstructure evolution, shrinkage, and characteristic densification phenomena;
- To assess the relationships between defects, microstructure and sintering parameters;
- To investigate the time-dependent change of material microstructure concerning coordination number and cohesive neck size distribution.

CHAPTER 2 – LITERATURE REVIEW

2.1 POWER TECHNOLOGY

Ceramic materials have been essential to human civilization for thousands of years, offering remarkable properties such as high hardness, excellent heat resistance, electrical insulation, and corrosion resistance (FURLAN, 2013; GERMAN, 2010). Powder technology is a versatile manufacturing process that has gained significant importance in producing a variety of materials. To meet the demands of modern technology and industry, powder technology has emerged as a promising technique for processing ceramic materials, which is mainly attributable to the cost savings associated with net (or near-net) shape processing compared to other processing methods (“European Power Metallurgy Association (EPMA)”, [s.d.]).

Unlike traditional melting and casting methods, powder technology focuses on creating ceramics from finely powdered raw materials. This approach enables the production of complex shapes with exceptional precision while also offering the possibility of tailoring the microstructure and properties of the final ceramic product. By controlling factors like particle size, distribution, and composition, engineers and researchers can achieve ceramic components with enhanced mechanical strength, superior thermal stability, and optimized performance for specific applications (GERMAN, 2010; RAHAMAN, 2003). The significant advantage of powder technology is the reduced powder loss and the low value of energy consumed during the process (per kilogram of produced part). For pieces with close tolerance dimensional and without the need for secondary operations, the value of raw material used versus the final product can reach 95%. The energy consumption for each kilogram of the produced part goes 29% against 66-82% in a parts production process through the machining (“European Powder Metallurgy Association”, [s.d.]). Figure 2.1 illustrates this panorama.

Figure 2.1: Comparison of raw materials utilization and energy required for various manufacturing processes.

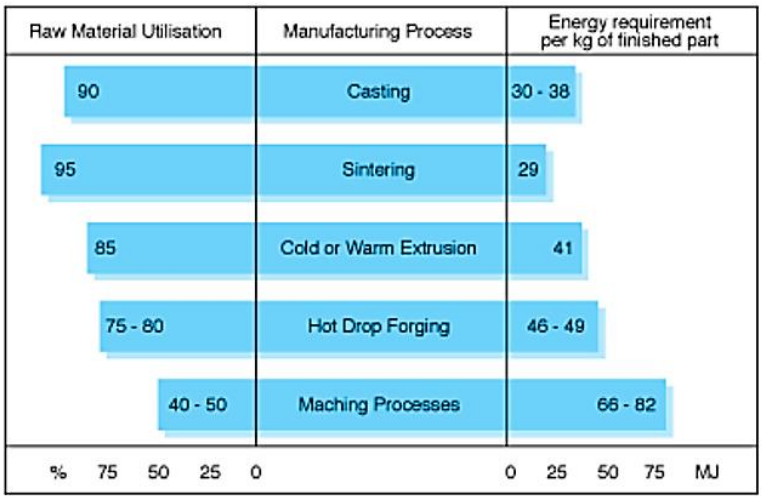

Source: EPMA, European Powder Metallurgy Association (EPMA) - Economic Advantages, accessed on July 23rd, 2023.

Moreover, powder technology opens new possibilities for developing advanced ceramic materials that may not be feasible through conventional methods (ALVES et al., 2021). Composite ceramics, for instance, can be engineered by blending different powders to combine the strengths of various materials, creating hybrids with unique characteristics. This range of possibilities has significant implications in industries ranging from aerospace and electronics to automotive and medical devices (FURLAN, 2013; RAHAMAN, 2003, 2007).

The powder technology process applied for ceramics typically involves powder preparation, shaping, and heating, as shown in Figure 2.2. Each step requires careful attention to detail to ensure the final product achieves the desired properties. Powder compaction and shaping techniques facilitate the formation of intricate ceramic components without extensive machining, reducing material wastage and overall production costs. The firing step, consisting of drying and sintering, is responsible for the densification and enhancement of the mechanical strength of the final ceramic product (REED, 1995).

Figure 2.2: Typical flowchart of the ceramic manufacturing process.

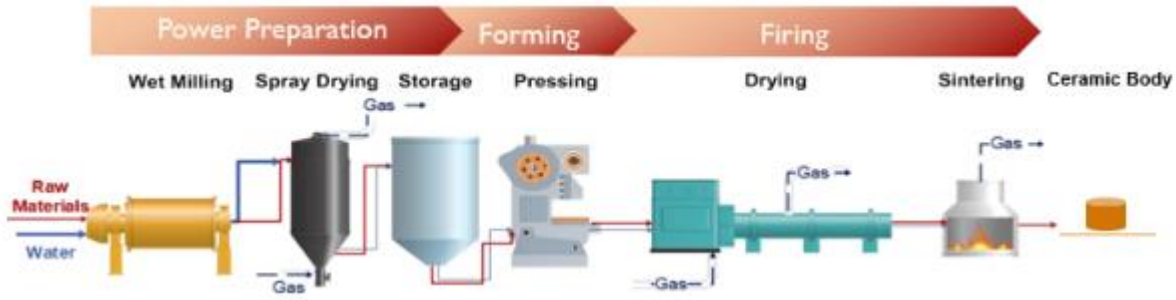

Source: Adapted from ALVES et al., 2021

2.2 FUNDAMENTAL CONCEPTS IN SINTERING

Sintering is a crucial step in the manufacturing of powder technology-based products. Almost all ceramic bodies must be fired at high temperatures to develop the microstructure with desired properties. This widespread use of the sintering process has led to various approaches to the subject. In practice, the ceramist, wishing to prepare a material with a particular set of properties, identifies the required microstructure. Sintering studies aim to understand how the processing variables influence the microstructural evolution during sintering. In this way, helpful information can be provided for designing processing conditions to produce the required microstructure (RAHAMAN, 2003).

According to German (GERMAN, 2010), sintering is a thermal process of joining particles through mass transport mechanisms that occur primarily at the atomic level. This process usually occurs at high temperatures, with or without liquid phase formation. The driving force is the reduction of the system's free energy, represented by the decrease of the curvatures on the surfaces of the powders and the elimination of the total surface area. It allows the production of solid materials (parts) from porous bodies composed of powder conglomerates by forming and growing bonds between particles and changing the geometry and size of pores (GERMAN, 2010; RAHAMAN, 2003). Sintering transforms a dispersed system with high free energy to a stable state with lower free energy and porosity. In the sintering stage, material retraction occurs, causing an increase in its relative density and the definition of its mechanical and physical properties. There is also a significant increase in hardness and mechanical strength and changes in ductility, conductivity (thermal and electrical), magnetic

permeability, etc., depending on the microstructural transformations (GERMAN; LATHROP, 1978; REED, 1995).

2.2.1 Types of sintering

Sintering can be classified from different aspects, such as technique, heating rate, and phases. Considering the solid-liquid-pore phases, content sintering processes can be divided into four categories, as illustrated in Figure 2.3.

- Liquid Phase Sintering (LPS), which involves all three components but is concentrated at the solid apex since most material is solid (<20% liquid) (KANG, 2010; MAHI; KWON, 2016; RAHAMAN, 2007);
- Viscous Glass Sintering (VGS), also termed viscous flow, is the glass powder densifying mechanism in glazing and enameling (L.KANG, 2005; RAHAMAN, 2003, 2007). This involves liquid (molten glass) and pores;
- Viscous Composite Sintering (VCS) or vitrification, where the liquid content is >20% corresponding to the region relevant to sinter whiteware such as porcelain (RAHAMAN, 2007; REED, 1995); and
- Solid State Sintering (SSS), which is covered by the right-hand edge involving only solids and pores (RAHAMAN, 2007; REED, 1995).]

Figure 2.3: Ternary solid-liquid-pore diagram showing different types of sintering.

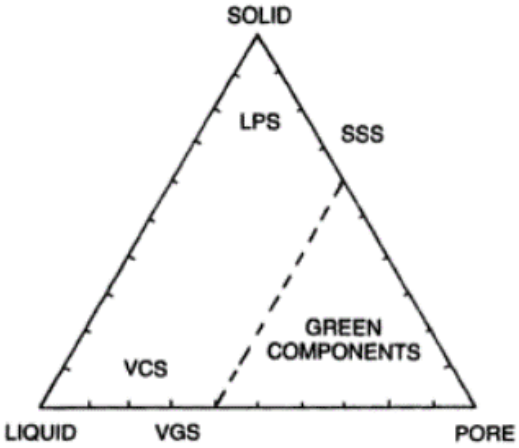

Source: REED, 1995.

2.2.2 Driving force and mechanisms of sintering

The driving force and the sintering mechanisms are different from each other. The driving force can be seen as a thermodynamic potential gradient, while the sintering mechanisms are associated with the ways of mass transport, which in turn define the sintering kinetics (FURLAN, 2013; GERMAN, 2010).

All movement of matter in a preferential direction takes place to decrease the gradients of thermodynamic potential. The main component of the driving force for sintering is the surface energy. From a macroscopic view, each reaction proceeds from the high-level energy to the minimum energy for solid-state sintering. Usually, the free energy is constituted of two parts: the interface energy and the total surface area. From a microscopic view, concave surfaces are under compressive stress, whereas convex surfaces are under tensile stress. However, flat surfaces are free of stress. Thus, atomic motion induces the concave region to fill the convex region (GERMAN, 2010).

The sintering mechanism describes how mass transport occurs (“Ferrous_Powder_Metallurgy”, [s.d.]; FURLAN, 2013). Matter is transported predominantly by diffusion of atoms, ions, or other charged species. Matter transport during sintering can occur by at least six different paths that define the sintering

mechanisms. Some mechanisms (referred to as densifying mechanisms) lead to the densification of the powder system, whereas others (non-densifying mechanisms) do not. In practice, more than one mechanism operates during any given sintering regime. All the mechanisms lead to the growth of the necks between the particles and influence the densification rate. In Figure 2.4, six different sintering mechanisms in polycrystalline materials are shown. As mentioned above, the neck's growth occurs by each mechanism. Only specific mechanisms, however, lead to shrinkage and densification. In these, matter is removed from grain boundaries (mechanisms 4 and 5) or dislocations within the neck region (mechanism 6). Mechanism 5 is called lattice diffusion or volume diffusion in different publications. Mechanisms 1-3 do not cause densification. However, these non-densifying mechanisms cannot be ignored because they reduce the curvature of the neck surface (i.e., the driving force for sintering) and reduce the rate of the densifying mechanisms (RAHAMAN, 2003, 2007).

Figure 2.4: Schematic illustration of the different sintering mechanisms.

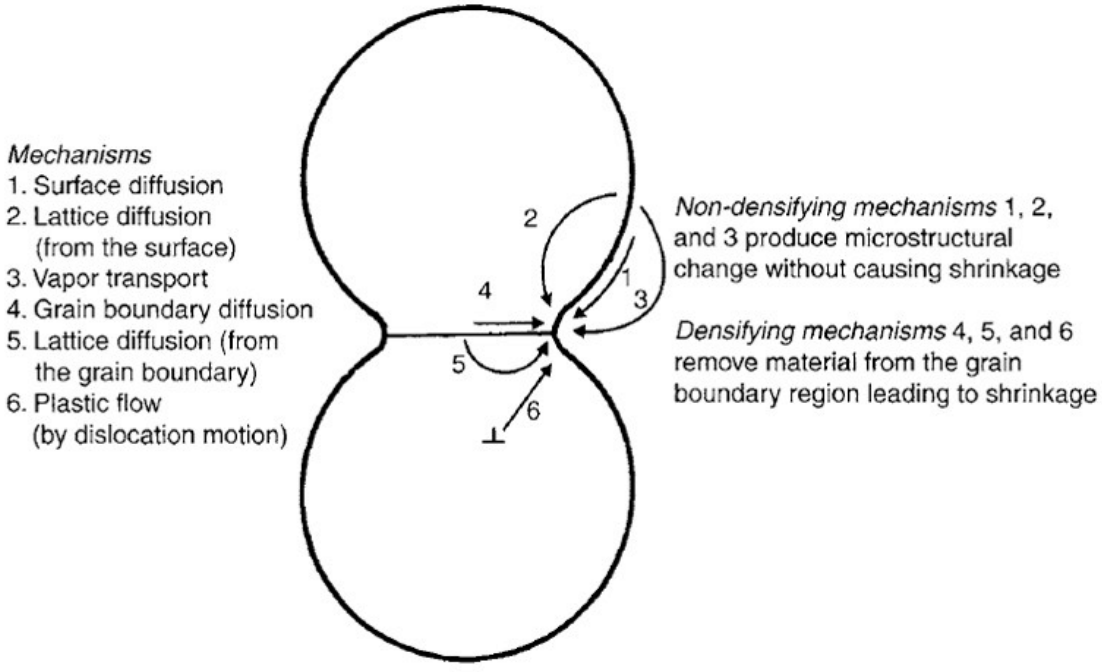

Source: RAHAMAN, 2003, 2007.

2.2.3 Solid-state sintering stages

Analytical models were developed for theoretical analysis and quantitative modelling of the sintering process Field (GERMAN, 2010; GERMAN; LATHROP, 1978). According to Coble (COBLE, 1958), solid-state sintering can be divided into three stages. A stage represents an interval of time or density over which the microstructure is reasonably well defined, as depicted in Figure 2.5:

I. Formation of “necks”: The contacts between the particles form “necks”, generating continuity of matter (GÓMEZ; HOTZA, 2018). In this step, the grain boundaries are created, fundamental for the densification process. The contact area between the particles increases from zero (ideally point contact) to ~0.4-0.5 of the particle radius. The significant initial differences in surface curvature are removed, and 3-5% of linear shrinkage occurs in this stage, thus yielding an increase to roughly 0.65 of the theoretical density. As Coble Field (COBLE, 1958) indicates, the initial sintering step involves no grain growth—the occurrence of a small dimensional retraction (REED, 1995).

II. Intermediate stage: It starts when grain boundaries are well formed. The ratio growth between the neck and particle radii occurs during this stage. It is possible to identify two “phases” in the material: the solid and void phases in an interconnected network of pores (GÓMEZ; HOTZA, 2018). Most densification and microstructure changes take place in this stage of sintering. As pores become isolated and grain boundaries form a continuous network, the intermediate sintering stage ends when a density of ~0.9 of theoretical density and the third or final sintering stage starts (GERMAN, 2010). Occurrence of sizeable dimensional shrinkage.

III. Final stage: Isolation and rounding of the pores (95 to 99% densities concerning the theoretical density of the material). If the pores contain gases not soluble, densification will be impaired due to the isostatic pressure exerted by the gas trapped in the pores. Density increases slightly, but the microstructure develops (grains grow) very rapidly in this stage of the sintering (GERMAN, 2010; REED, 1995).

Figure 2.5: Illustration of sintering stages.

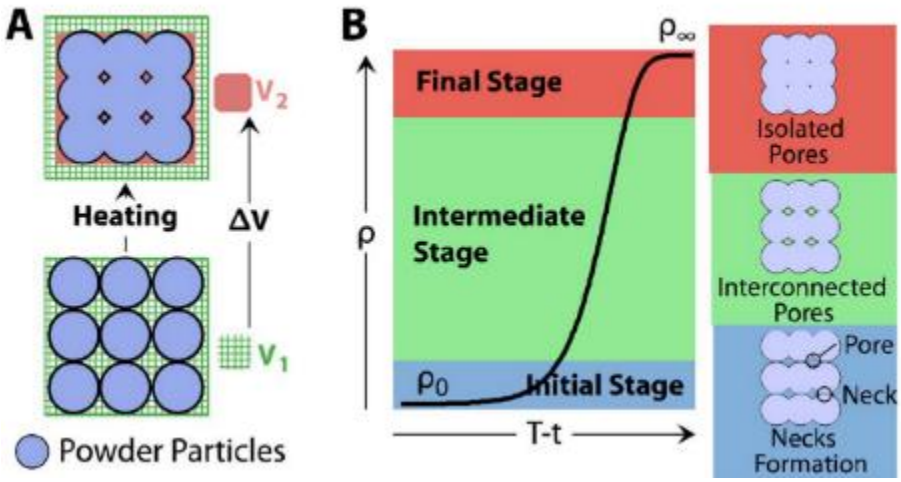

Source: GÓMEZ; HOTZA, 2018.

The sintering cycle is composed of four events: heating and cooling rate(s), hold temperature(s) and hold time(s). Each of these events influences the final properties.

The heating rate influences the sintering kinetics, determining whether the desired transformations occur within a predetermined temperature range (or time) and whether this transformation is stable. A high heating rate (on the order of 20-25 °C/min) can cause component failure (when thermal stresses exceed the strength of the molded component). It is essential to assess whether a given rate is economically viable, as the ideal rate is not always possible to use (RAHAMAN, 2003, 2007).

The sintering threshold temperature directly influences the diffusive flux within the component. Higher temperatures are desired, as with increasing temperature, there is an increase in the diffusion coefficient (FURLAN, 2013).

Higher sintering temperatures can lead to component distortion (due to the component's low mechanical resistance to plastic deformation at high temperatures, together with the action of green density gradients and the gravitational force on it), thermal decomposition of some phases, and eventual reduction of oxides. (CHU et al., 1991; GERMAN, 2010; LIN; DE JONGHE; RAHAMAN, 1997; RAHAMAN, 2007).

2.3 DISCRETE ELEMENT METHOD - DEM

In the field of numerical modelling, many methods have been developed for application to continuous or discrete systems, such as Boundary Element Method (BEM), Finite Element Method (FEM), Finite Difference Method (FDM), and Discrete Element Method (DEM). Each method has limitations and advantages. The choice of a technique depends on the physical nature of the problem and its conditions (HOGUE et al., 2008; RIERA; MIGUEL; ITURRIOZ, 2016). For powder materials, the DEM has become popular.

The roots of the Discrete Element Method can be traced back to the 1950s when the mathematician and physicist Richard Feynman proposed a simple model to study the motion of granular materials. However, it was in the 1970s that the method took a more structured form with the works of Cundall and Strack, who independently introduced the concept of simulating discrete particles using numerical methods. The method was used initially for problems involving rock fractures. Their initial application aimed at two-dimensional work in which rigid particles were treated as discs or spheres (BURMAN; CUNDALL; STRACK, 1980; RIERA; MIGUEL; ITURRIOZ, 2016). Their seminal contributions laid the foundation for what is now known as the Discrete Element Method.

The fundamental difference between the DEM method concerning other methods is the interaction particle by particle. The DEM method takes finite particles, and each particle is treated individually by Newton's equation of motion and force-deformation law for the contact between particles (COETZEE; ELS, 2009). This makes the system “discrete”, which is why the method is called the Discrete Element Method. The positions, velocities, and accelerations are updated by calculating the contact forces between them after each interaction, that is, at each time step. The method can include models for interparticle contacting forces, magnetic force, electrostatic, gravitational, sintering, etc. (BURMAN; CUNDALL; STRACK, 1980; ROCK; ZHANG; DAVID WILKINSON, 2008).

The main advantages of DEM (ROCK; ZHANG; DAVID WILKINSON, 2008) lie on the understanding of every individual behavior that contributes to macro features, flexibility and extension capability. DEM is designed for more dynamic problems such as vibration problems, propagation of waves, contacts, etc. Due to this feature, it can be easily modified to solve other issues, such as heat transfer with thermal resistance

and static problems with relaxation. Applications for the method guided the fields of geology, mining industries, soil mechanics, geotechnical engineering, civil engineering, powder technology, food industries, etc. The technique presents satisfactory accuracy in simulating flows of granular solids. Avalanche studies, problems with mining, and rock faults are also method extensions. It is currently highlighted in the ranking of granular media, whose assessments occur both in academia and industry.

However, Rock and Wilkinson (ROCK; ZHANG; DAVID WILKINSON, 2008) also point out the difficulty of obtaining global mechanical responses as a limitation of DEM. As the domain is discretized into particles with different parts in contact with each other, the result from the entire assembly of particles is complex. Moreover, a drawback of discretizing every particle is the computational expense, which often limits the size of the system under analysis.

2.3.1 Basic DEM routine

The calculation cycle of the DEM algorithm mainly consists of 6 steps (ROCK; ZHANG; DAVID WILKINSON, 2008) as described below and represented in Figure 2.6:

- Particle Generation: Define the initial positions, shapes, and properties of the individual particles or bodies within the system;
- Time Integration: Employ numerical integration techniques to update the positions and velocities of particles over small time steps;
- Contact Detection: Identify and analyze interactions between particles, considering factors like overlapping and relative velocities;
- Force Calculation: Compute contact forces and torques between particles based on their interactions and material properties;
- Update Particle Motions: Using Newton's laws of motion, update the positions and velocities of particles considering the forces acting on them;
- Repeat and Iteration: Repeat the time integration and force calculations over successive steps until the desired simulation time is reached.

Figure 2.6: The steps of the basic routine of the Discrete Element Method.

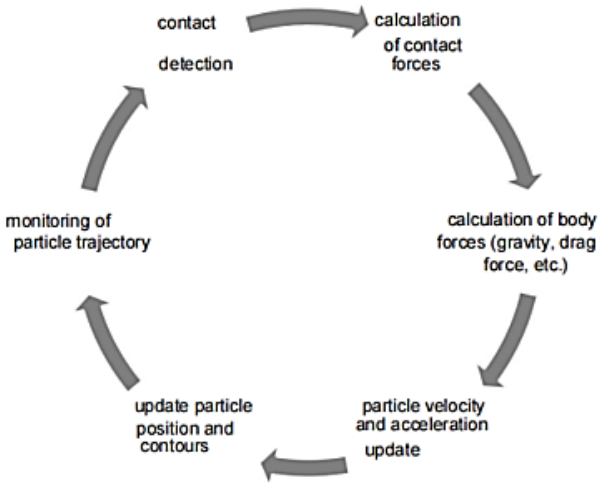

Source: SANTOS et al., 2014.

2.3.2 Sintering forces

Sintering contact forces are given by Parhami & Mc Meeking's model (PARHAMI; MCMEEKING, 1998), which considers surface and grain-boundary diffusion the main densification mechanisms. For two spherical particles of the same radius, the normal force F_N [N] (Equations 2.1-2.3) is expressed as a sum of attractive and viscous forces:

$$F_N = F_{atractive} + F_{viscous} \quad (2.1)$$

$$F_{atractive} = \frac{\alpha}{\beta}\,\pi\, r\, \gamma_s \quad (2.2)$$

$$F_{viscous} = -\frac{\pi}{2\,\beta\, D}\, r_c^4 v_{rel,N} \quad (2.3)$$

where *α* and *ß* are parameters of the model, *r* is the radius of particles [m], γ_s is the surface energy [J m^{-2}], r_c is the contact radius [m], *D* is the coefficient of diffusion [m^2 s^{-1}] and $v_{rel,N}$ is the relative velocity in the normal direction [m s^{-1}].

The tangential contact force F_T [N] opposes the tangential component and mainly depends on the relative velocity in tangential direction $v_{rel,T}$ [m s^{-1}] as described in Equation 2.4:

$$F_T = -\eta \frac{\pi R^2}{2 \beta D} r_c^2 v_{rel,T} \quad (2.4)$$

where η is a dimensionless viscous coefficient that describes the resistance to slip (viscosity) of particle-particle contacts, it was assumed within this model that the contacts are large enough to oppose any rotation of the particles.

The parameters α and ß depend on the ratio of the grain-boundary diffusion ($\delta_b D_b$) to the surface diffusion ($\delta_s D_s$) as in the following relation:

$$\varphi = \frac{\delta_b D_b}{\delta_s D_s} \quad (2.5)$$

According to Martin and Bordia (MARTIN et al., 2009; MARTIN; BORDIA, 2009), ß = 4 can be used for all values. For α = 9/2, grain-boundary diffusion is considered the sintering dominant mechanism, influencing densification two times higher than the surface diffusion. Whereas α = 5/2 is suitable for simulated sintering when surface diffusion prevails over grain-boundary diffusion.

The contact radius was calculated by Equation 2.6 according to Coble's geometric model (COBLE, 1958). The material confined in the overlapping region is redistributed to form the sintering neck.

$$r_c = \sqrt{2 R \xi} \quad (2.6)$$

where R is the particle radius, and ξ is the overlapping [m], computed as the sum of the particle's radii diminished by the distance between the centers of contact partners. Note that $F_{viscous}$ (Equation 2.3) may be tensile or compressive depending on the relative velocity in the contact ($v_{rel,N}$). Likewise, the viscous term depends on the size of the contact radius r_c to the power of fourth, leading to a very large viscosity for large contacts.

The diffusion parameter D [$m^2\ s^{-1}$] (Equation 2.7) is defined as a function of the atomic volume Ω [m^3], the Boltzmann constant k [$m^2\ kg\ s^{-2}\ K^{-1}$], the sintering temperature T [K], the grain-boundary thickness δ_b [m] and diffusion coefficient for vacancy transport D_b [$m^2\ s^{-1}$]. This last one (D_b) is accounted by an Arrhenius-type relationship (Equation 2.8), where D_{0b} is the maximum diffusion coefficient [$m^2\ s^{-1}$], Q

is the activation energy [J mol^{-1}], R_g is the universal gas constant [J mol^{-1} K^{-1}]and T is the sintering temperature [K].

$$D = \frac{\Omega}{k\,T}\,\delta_b\,D_b \tag{2.7}$$

$$D_b = D_{0b}\,e^{\frac{-Q}{R_g\,T}} \tag{2.8}$$

Notice that the described model does not consider grain growth, friction, or heat transfer during sintering. Moreover, DEM only treats pair interaction, i.e., particles with null coordination numbers are not further considered in the model. Therefore, the volume redistribution (from the overlapping to the neck) is not exact anymore.

CHAPTER 3 – HIGH HEATING RATE SINTERING AND MICROSTRUCTURAL EVOLUTION ASSESSMENT USING THE DISCRETE ELEMENT METHOD[1]

3.1 INTRODUCTION

Sintering is a process where a substance in a dispersed state is transformed into a solid body with a higher density. It is a critical step in the microstructural development of parts produced by powder technology (GERMAN, 2010; GERMAN; LATHROP, 1978; GRUPP et al., 2011). Fast heating rates have attracted scientific and technological interest to obtain highly dense ceramics with fine-grained microstructure in periods as short as some minutes (GÓMEZ et al., 2016; POSSAMAI et al., 2012). The main technological advantages of fast firing lie in the economic and environmental benefits of lower energy consumption per payload, lower emissions, reduced scrap and re-fire, lower labor costs, shorter production times, and more reliable product consistency (CAMM, 2017; GHORRA, 2008; SINGH; SUBRAHMANYAM, 1976). Experimental procedures on fast firing ceramic systems are vastly found in the literature (BERNARDO; SCARINCI, 2008; DONDI; MARSIGLI; VENTURI, 1999; DUTRA et al., 2009; GARCÍA et al., 1995; PINTO; SOUSA; HOLANDA, 2005; SEAL et al., 2006; ZHANG et al., 2010). These studies focus on hardness, relative density, water absorption, bending strength, and microstructural features, essentially grain growth and phase evolution. García and collaborators (GARCÍA; HOTZA; JANSSEN, 2011) experimentally assessed the thermal gradients generated through an Al_2O_3 body and the resultant densification front throughout a fast-sintering protocol. However, the determination of the thermal gradients was limited to low temperatures (up to 1050 ºC). Thus, despite the significant progress in the area, it has been challenging to fully understand the rearrangement, the densification, and the heat transfer phenomena on particulate systems under rapid sintering via experimentation only. Numerical approaches have played a crucial role in elucidating thermomechanical phenomena, contributing to the control and optimization of the materials processing chain. Namely, the finite element method (FEM), the finite volume method (FVM) and the discrete element method (DEM) have been applied to model thermal phenomena in fluidized

[1] Published in Open Ceramics https://doi.org/10.1016/j.oceram.2021.100182

and packed beds (ANDERSON et al., 2015; CHEN et al., 2019; FENG; HAN; OWEN, 2009; HADDAD et al., 2021; HADDAD; GUESSASMA; FORTIN, 2014; KIANI-OSHTORJANI; JALALI, 2019; MOSCARDINI et al., 2018; ROUSSEAU et al., 2014; SANGRÓS; SCHILDE; KWADE, 2016; TERREROS; IORDANOFF; CHARLES, 2013; TSUJI; TANAKA; ISHIDA, 1992; VARGAS; MCCARTHY, 2002; WANG et al., 2020; WU et al., 2017; ZHOU; ZHANG; ZHENG, 2012)(ANDERSON et al., 2015; CHEN et al., 2019) as well as for modeling of isothermal sintering (BESLER et al., 2015, 2016; DOSTA et al., 2020; JAUFFRÈS et al., 2012; MORI, 2006; RASP et al., 2017; RASP; KRAFT; RIEDEL, 2013). Nevertheless, scarce numerical studies on fast firing, based on FEM and FVM essentially, are found in the literature (GANERIWALA; ZOHDI, 2016; MORI, 2006; POSSAMAI et al., 2012). Besides, in most cases, unrealistic assumptions are made, such as considering the green ceramic a non-porous body and the absence of shrinkage during the densification. Furthermore, the FEM and FVM are well known element-based approaches for continuum media. Thus, the behavior of individual particles is neglected by design, and the discretization of small particles in the mesh may have its accuracy diminished by the loss of microstructural information (GANERIWALA; ZOHDI, 2016; POSSAMAI et al., 2012; RASP; KRAFT; RIEDEL, 2013). The DEM approach overcomes the issues by accounting for the granulated nature of the powder that composes the green body. Each powder particle can be considered a discrete unit that interacts with its neighbors according to the appropriate sintering laws. This method offers the advantage of considering grain rearrangement effects by design (HENRICH et al., 2007). It also allows accessing micro/mesoscopic properties such as position, velocity, contact area, and coordination number of every particle (WEBER et al., 2017). Many DEM-based studies of sintering processes were performed using the model proposed by Parhami & McMeeking (PARHAMI; MCMEEKING, 1998) for free and pressure-assisted isothermal sintering. This model has been extensively applied to model particles (C. L.MARTIN et al., 2006; HENRICH et al., 2007; JAUFFRÈS et al., 2012; MARTIN et al., 2014, 2016b) and pores (BESLER et al., 2015; DOSTA et al., 2020) rearrangement, anisotropic (HENRICH et al., 2007; LICHTNER et al., 2018) and constrained (DUTRA et al., 2009; RASP et al., 2017) sintering, as well as the evolution of heterogeneities/defects during sintering. The Parhami & McMeeking model (PARHAMI; MCMEEKING, 1998) was extended to describe grain coarsening (C. L.MARTIN et al., 2006; PARHAMI et al., 1999), to consider variable coordination numbers (RASP; KRAFT; RIEDEL, 2013), and to model

the elastic component of sintering besides viscous flow (NOSEWICZ et al., 2013, 2017; NOSEWICZ; ROJEK; CHMIELEWSKI, 2020). Lately, it was applied to the modeling of composites sintering (BESLER et al., 2016; IACOBELLIS; RADHI; BEHDINAN, 2019; NOSEWICZ; ROJEK; CHMIELEWSKI, 2020). Note that none of the preceding approaches addressed sintering under non-isothermal conditions, i.e., fast sintering, in which the high heating rates generate gradients of temperature that contribute significantly to microstructure development, densification, and final product properties. In this contribution, we present an original model for coupling Thermo-Mechanics with Sintering model (TMS) to further understand the thermo-micromechanical behavior of particulate systems and their microstructure evolution during sintering, especially under the no isothermal procedure. The TMS model was developed based on the DEM and applied on a ceramic body of Al_2O_3. The main equations and assumptions were consistently described. Microstructural and thermal features were compared with experimental data. Relationships between defects, microstructure, and sintering parameters were explored. The time-dependent change of material microstructure concerning coordination number, cohesive neck size, gradients of temperature and sample length are also analyzed. The simulation framework MUSEN (DOSTA; SKORYCH, 2020) was used to perform the simulations, an open-source software widely used in DEM investigations (BESLER et al., 2015, 2016; DOSTA et al., 2020; DRANISHNYKOV; DOSTA, 2019; KOZHAR et al., 2015; WEBER et al., 2017). This system supports parallel computing on GPU based on the CUDA platform, which significantly reduces computation time, thus efficiently simulating millions of discrete objects (DOSTA et al., 2020; DOSTA; SKORYCH, 2020).

3.2 THERMO-MECHANICS COUPLED WITH SINTERING (TMS) MODEL

3.2.1 Problem set-up

A transient heating process was assumed to determine the temperature field inside the solid body. Fast firing simulations were carried out in the temperature range of 1250–1350 C. An instantaneous heating rate was applied to resemble the direct introduction of the sample into a pre-heated furnace at sintering temperature. Further decreases in the heating rate were considered to evaluate its relationship with microstructural development. The furnace was modeled only by the boundary

conditions applied to the body surface. Its temperature was assumed to remain constant over the process, and heat losses between the sample and the enclosed environment were neglected.

The proposed TMS model was applied to an Al_2O_3 system and validated with previously published experimental results. The numerical sample was designed to preserve particle size and scale the compact dimensions down due to computational limitations. The specific heat capacity $c_p(T)$ and thermal conductivity $\kappa(T)$ of alumina were temperature-dependent [57] according to Equations 3.1 and 3.2:

$$c_p(T) = 1117 + 0.14\,T - 411\,e^{-0.006\,T} \quad (3.1)$$

$$\kappa(T) = 5.85 + \frac{15360\,e^{-0.002\,T}}{T + 516} \quad (3.2)$$

where T is the particle temperature (°C).

Applying the TMS model, thermal and relative density gradients were assessed and correlated with the microstructure evolution. Moreover, defects were purposefully introduced inside the Al_2O_3 compact addressing their influence on the final microstructure and relationship with sintering parameters. Lastly, micromechanical features were estimated based on the evolution of the coordination number and the cohesive neck size distribution.

3.2.2 Heat transfer phenomena

Heat transfer was approached as a thermomechanical problem. The particles were assumed to be opaque grey emitting spherical bodies with identical chemical compositions. Only thermal energy was transferred. The production/consumption of heat due to chemical reactions and thermal expansion were neglected. The determination of a temperature field for each particle is computationally unfeasible since granular assemblies contain many objects. Therefore, the isothermal premise was adopted in which each particle has one temperature degree of freedom only. The TMS model considered the following heat transfer mechanisms:

- Radiation – among particles at the sample surface and their surroundings, which corresponds to furnace environment;
- Convection – between the stagnant air inside the furnace and particles on the sample surface;
- Conduction – pair-wise heat transfers between contacting particles.

The particles were grouped in two zones based on their position to consider the different heat transfer mechanisms: the outer layer where all the heat transfer mechanisms are active and the inner zone, where only interparticle conductive heat transfer occurs. Radiative and convective heat transfer was approximated to happen in the exposed area Ap of outer particles solely. Figure 3.1 depicts the half-section view of the numerical sample highlighting the outer layer and the inner zone, along with an illustration of the heat transfer mechanisms considered in the TMS model.

Figure 3.1: Half section view of the 3D simulation sample highlights the outer and inner layers and illustrates the heat transfer mechanisms recognized in the TMS model. The arrows schematically depict the direction of heat flow. The heat flows from the hot environment surrounding (furnace atmosphere) to the outer particles through their representative contact area Ap. As the outer particles increase their

temperature, heat is transferred particle by particle to the inner zone along the ceramic body through the interparticle contact with radius r_c.

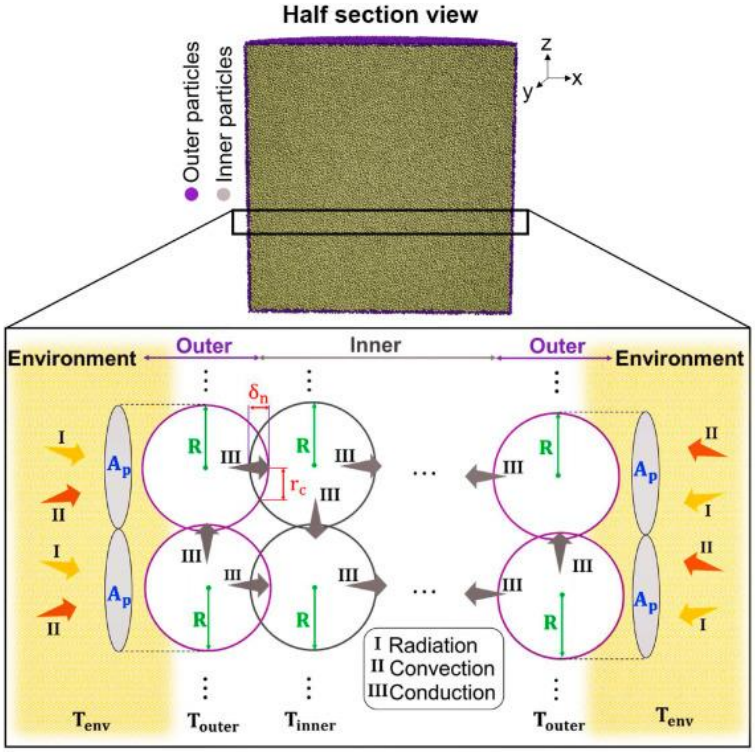

3.2.2.1. Radiation

The amount of thermal energy emitted by the environment and absorbed on outer particles surface was calculated by the Stefan Boltzmann law assuming isothermal surfaces (Equation 3.3). For the sake of simplicity and to reduce computational complexity, the representative contact area Ap (m^2) was approximated as the projection of each outer particle surface area facing the enclosing environment [39] as shown in Equation 3.4:

$$Q^{rad} = \varepsilon \, \sigma \, A_p \, S_a (T_{env}^4 - T_{outer}^4) \quad (3.3)$$

$$A_p = \pi \, R^2 \quad (3.4)$$

where Q_{rad} is the heat transfer rate by radiation (W), ε is the surface emissivity (−), σ is the Stefan-Boltzmann constant (W/m^2K^4), S_a is the parameter of scaling for mass-surface-dependent heat transfer (−), T_{env} is the environment temperature (K), Touter is the outer particle temperature (K), and R is the particle radius (m). The detailed

description of S_a is provided in Section 3.2.4.2. Equation 3.3 admits that the furnace cavity is considered a black body, and the radiative heat rate is uniformly distributed over the outer particles.

3.2.2.2 Convection

The convective heat transfer rate $\mathrm{Q}^{\mathrm{conv}}$ (W) was calculated according to Newton's law of cooling (Equation 3.5) (BERGMAN; LAVINE, 2017; GANERIWALA; ZOHDI, 2016; PENG; DOROODCHI; MOGHTADERI, 2020; POSSAMAI et al., 2012).

$$\mathrm{Q}^{\mathrm{conv}} = \mathrm{A_p}\ S_a\ \mathrm{h_c}(\mathrm{T_{env}} - \mathrm{T_{outer}}) \tag{3.5}$$

where $\mathrm{h_c}$ is the convective heat transfer coefficient, typically in the range of 2–25 W/m^{2}K for free convection in the air (BERGMAN; LAVINE, 2017). $\mathrm{A_p}$ and S_a are defined similarly as for radiation.

3.2.2.3 Conduction

The heat transfer rate by conduction $\mathrm{Q}^{\mathrm{cond}}$ (W) in the contact between particles i and j was modeled by Equation 3.6 (BATCHELOR; O'BRIEN, 1977; BERGMAN; LAVINE, 2017; LIANG; LI, 2014; VARGAS; MCCARTHY, 2002). The contact radius $\mathrm{r_c}$ (m) was derived from Coble geometric model (Equation 3.7) (BESLER et al., 2015; COBLE, 1958; MARTIN et al., 2016a). Note that i and j can be two outer particles, two inner particles, or an inner-outer contacting pair.

$$\mathrm{Q}^{\mathrm{cond}} = 2\ \mathrm{r_c} \cdot S_\ell \cdot \mathrm{f_{res}}(\delta_\mathrm{n}) \cdot \kappa(\mathrm{T}) \cdot (\mathrm{T_j} - \mathrm{T_i}) \tag{3.6}$$

$$\mathrm{r_c} = \sqrt{2\ \mathrm{R}\ \delta_\mathrm{n}} \tag{3.7}$$

where S_ℓ is a scaling parameter for mass-length-dependent heat transfer (-), $\kappa(\mathrm{T})$ is the temperature-dependent thermal conductivity (W/m·K) of the particles, $\mathrm{T_i}$ and $\mathrm{T_j}$ are the temperatures (K) of particles, $\mathrm{f_{res}}(\delta_\mathrm{n})$ is the thermal conduction resistivity facto, and δ_n is the normal overlap (m) estimated as the sum of particle's radii diminished by

the distance between the centres of contacting partners (s. Appendix). The calculation of S_ℓ is presented in Section 3.2.4.2.

The existence of surface heterogeneities in the Al_2O_3 powder can restrict the effective contact area to a small fraction of the nominal contact area. The resistance to heat transfer at these contacts is often amplified (ASKARI; HEJAZI; SAHIMI, 2017; BAHRAMI; CULHAM; YOVANOVICH, 2004; PENG; DOROODCHI; MOGHTADERI, 2020) as a consequence. Thus, a resistivity factor f_{res} was included to consider this effect and was fitted to experimental data. Here the three different regimes were distinguished (Equation 3.8):

- Initial contact formation: at the early sintering stages, when the overlap is smaller than the minimum threshold $\lambda_{min}R$, the conduction is limited by f_{res}^*;
- Transition zone: as overlaps increase due to sintering, interparticle contacts become more effective. Hence, f_{res} effect gradually loses its importance. Accordingly, the thermal conductivity of contacting particles is linearly increased to the effective value in the range between $\lambda_{min}R$ and $\lambda_{max}R$;
- Late stages: when the upper limit of an overlap $\lambda_{max}R$ is reached.

$$f_{res}(\delta_n) = \begin{cases} f_{res}^*, \sigma_n \leq \lambda_{min}R \\ f_{res} + \left(\frac{1 - f_{res}}{\lambda_{max} - \lambda_{min}}\right)\left(\frac{\delta_n}{R} - \lambda_{min}\right), \lambda_{min}R < \sigma_n < \lambda_{max}R \\ 1, \lambda_{max}R < \sigma_n \end{cases} \quad (3.8)$$

The conductive heat transfer model assumed quasi-static contacts, and conduction by a stagnant interstitial medium was neglected under the assumption of having much smaller thermal conductivity than the particles.

3.2.2.4 Global heat transfer

The overall heat $\dot{Q}_{tot}$ (Equation 3.9) transferred to a single particle may be expressed as the sum of each thermal exchange experienced.

$$\dot{Q}_{tot} = \dot{Q}^{rad} + \dot{Q}^{conv} + \sum \dot{Q}^{cond} \quad (3.9)$$

Thus, the energy conservation equation for every particle at each time-step was calculated by Equation 3.10.

$$m_p c_p(T) \frac{dT}{dt} = \dot{Q}^{rad} + \dot{Q}^{conv} + \sum \dot{Q}^{cond} \quad (3.10)$$

where m_p (kg) is the particle mass.

Thereby, the incremental temperature change $T(t + \Delta t)$ (Equation 3.11) of a single particle at each time-step Δt was computed by increasing its previous temperature $T(t)$ by the overall heat transfer.

$$T(t + \Delta t) = T(t) + \Delta t \frac{\dot{Q}_{tot}}{m_p c_p(T)} \quad (3.11)$$

3.2.3 Interparticle interaction

Different contact models were used for the modeling of particle-particle interactions. Either the non-isothermal sintering model, the modified Hertz-Mindlin, or repulsive force contact models were applied depending on two parameters: the average temperature of contacted particles $\overline{\mathrm{T}}$ and the normalized neck radius $\mathrm{r_c/R}$.

As sintering is a thermally activated process, it is consistent (in a mono-sized single-phase system) to consider a minimum temperature at which its mechanisms begin to activate. García et al. (GARCÍA; HOTZA; JANSSEN, 2011) found out that up to 1050 ºC, powder compacts of ultrafine alumina particles (~0.2 μm) showed no evidence of significant dimensional changes, that is, sintering mechanisms seemed to be still inactive up to this temperature. Hence, this temperature threshold has been implemented as a minimum temperature $\mathrm{T_{min}^{sint}}$, below which no sintering occurs.

The relative density can be calculated using the evolution of $\mathrm{r_c}$ (COBLE, 1958). Thereby, a stop criterion for densification was defined based on the dimensionless parameter $\mathrm{r_c/R}$, which was derived by normalizing the contact radius $\mathrm{r_c}$ over the particle radius R. Exploratory simulations confirmed that a fully dense sample was achieved at $\mathrm{r_c/R} = 0.8$. Note that $\mathrm{r_c/R}$ is neither material nor number of particles dependent. The application of each contact model according to the specified conditions is expressed by Equation 3.12.

$$\begin{cases} \overline{\mathrm{T}} < \mathrm{T_{min}^{sint}} & \mathrm{Hertz-Mindlin} \\ \overline{\mathrm{T}} \geq \mathrm{T_{min}^{sint}} \text{ and } \frac{\mathrm{r_c}}{\mathrm{R}} \leq 0.8 & \mathrm{Sintering\ forces} \\ \overline{\mathrm{T}} \geq \mathrm{T_{min}^{sint}} \text{ and } \frac{\mathrm{r_c}}{\mathrm{R}} > 0.8 & \mathrm{Repulsive\ force} \end{cases} \tag{3.12}$$

3.2.3.1 Contact model

For low temperatures $\left(\overline{\mathrm{T}} < \mathrm{T_{min}^{sint}}\right)$ at which sintering mechanisms are inactive, the modified non-linear Hertz-Mindlin contact force model was applied to allow particles to have rotational and translational degrees of freedom (DI RENZO; PAOLO DI MAIO, 2005; MINDLIN; DERESIEWICZ, 1953; TSUJI; TANAKA; ISHIDA, 1992). The formulated rheological model (MINDLIN; DERESIEWICZ, 1953; TSUJI; TANAKA; ISHIDA, 1992), illustrated in Figure 3.2, treated particle interaction as a viscoelastic

contact consisting of elastic stiffness K and viscous damping B components in normal $\mathrm{F_n^{HM}}$ (Equation 3.13) and tangential $\mathrm{F_t^{HM}}$ (Equation 3.14) directions.

Figure 3.2: Illustration of particle-particle contact forces in tangential and normal directions.

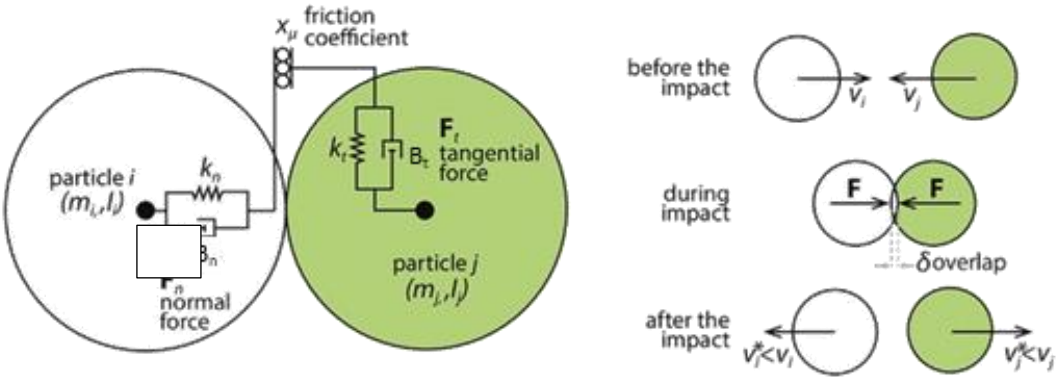

Note that both K and B parameters depend on the normal overlap (s. Appendix – Eqs. A.2-5).

$$\mathrm{F_n^{HM}} = \mathrm{K_n}\delta_\mathrm{n}^{\mathrm{HM}} - \mathrm{B_n}\mathrm{v_{rel,n}} \tag{3.13}$$

$$\mathrm{F_t^{HM}} = \mathrm{K_t}\delta_t - \mathrm{B_t}\mathrm{v_{rel,t}} \tag{3.14}$$

where $\delta_\mathrm{n}^{\mathrm{HM}}$ and δ_t are the interparticle overlaps (m) in normal and tangential directions. Compared to the standard formulation of the Hertz-Mindlin model, where the normal overlap is calculated based on the particle positions and their radii only, the present model incorporated an additional parameter δ_pl to describe flattening of initial contact surface and further “plastic” deformation caused by material sintering. The resulting normal overlap was calculated as Equation 3.15:

$$\delta_\mathrm{n}^{\mathrm{HM}} = \delta_\mathrm{n} - \ \delta_\mathrm{pl} \tag{3.15}$$

After the densification stage, particles in the initial packing, which represent the green body, may have significant overlaps, and the direct application of the Hertz-Mindlin model may cause unphysical initial stresses. To avoid them, Equation 3.16 was applied to consider all initial overlaps as initial flattening of the contact surface. The

initial plastic deformation was calculated based on the particle positions at the initial time step.

$$\delta_{pl} = R_i + R_j - |\vec{X}_i(t_0) - \vec{X}_j(t_0)| \quad (3.16)$$

When the average temperature at the interparticle contact is larger than the sintering temperature ($\overline{T} \geq T_{min}^{sint}$), and the overlap is larger than the predetermined threshold (s. Equation 3.12), then only the repulsive force acts between the particles. This force was introduced to avoid sample over-densification, which could lead to non-physical negative porosities. The repulsive force acted in normal direction and the overlap was calculated as:

$$F_n^{rep} = K_n \delta_n^{rep} - B_n v_{rel,n} \quad (3.17)$$

$$\delta_n^{rep} = \delta_n - \delta_{max} \quad (3.18)$$

where δ_{max} is the maximal interparticle overlap in the fully densified state. This parameter has been identified as 80% of particle radius.

3.2.3.2 Non-isothermal solid-state sintering

When particles' temperature is high enough ($\overline{T} \geq T_{min}^{sint}$), sintering starts. It is supposed that all the mechanical stresses previously caused due to compression or tension are relaxed and δ_{pl} is equaled to δ_n. Given account for non-isothermal conditions, the mass transfer parameter Δ_b ($m^4 \cdot s/kg$) was discretized as a function of the average temperature $\overline{T}$ (K) of every pair-wise contacting particle at each time step (Equation 3.19).

$$\Delta_b = \frac{\Omega}{\kappa_B \overline{T}} \delta_b D_{0b} e^{\frac{-Q_b}{R_g \overline{T}}} \quad (3.19)$$

where Ω is the atomic volume (m^3), κ_B is the Boltzmann constant ($m^2 \cdot kg/K \cdot s^2$), δ_b is the grain boundary thickness (m), D_{0b} is the diffusion coefficient (m^2/s), Q_b is the activation energy (J/mol), and R_g is the universal gas constant ($J/K \cdot mol$).

The average temperature $\overline{T}$ was computed by Equation 3.20, where T_i and T_j are the temperatures of contacting particles.

$$\overline{T} = \frac{T_i + T_j}{2} \tag{3.20}$$

With the activation of sintering, forces in the normal F_n^{sint} (N) and tangential F_t^{sint} (N) directions appear (MARTIN et al., 2009; PARHAMI; MCMEEKING, 1998). Sintering normal force (Equation 3.21) consisted of an attractive component, leading to densification, and a dissipative part, acting against the relative motion of the particles.

$$F_n^{sint} = F_{attractive} + F_{dissipative} = \frac{\alpha}{\beta}\pi R\gamma_s - \frac{\pi}{2\beta\Delta_b} r_c^4 v_{rel,n} \tag{3.21}$$

where α and β are model parameters (-) related to the dominant mass transport mechanism, γ_s is the surface energy of particles (J/m^2), and $v_{rel,n}$ is the relative velocity (m/s) of the particles in the normal direction. Parameters α and β depend on the ratio of the grain boundary to the surface diffusion. According to Bouvard & McMeeking calculations (BOUVARD; MCMEEKING, 1996), $\beta = 4$ may be used in all the cases. The parameter $\alpha = 9/2$ is applicable when grain-boundary diffusion is considered as a dominant sintering mechanism, whereas $\alpha = 5/2$ is suitable when surface diffusion prevails over grain-boundary diffusion. Grain-boundary diffusion was assumed to be the dominant mechanism of mass transfer during the sintering of Al_2O_3 (BESLER et al., 2015; MARTIN et al., 2009; RAETHER; SCHULZE HORN, 2009; RASP et al., 2017). Besides, it was previously demonstrated that the dihedral angle has a limited effect on α and β (BOUVARD; MCMEEKING, 1996; MARTIN; BORDIA, 2009); therefore, it was neglected here. The contact radius r_c was calculated as previously stated in Equation 3.7.

The tangential sintering force F_t^{sint} consisted of a dissipative component opposing to the relative motion in the tangential direction $v_{rel,t}$ (m/s), as shown in Equation 3.22.

$$F_t^{sint} = -\eta \frac{\pi R}{\beta\Delta_b} r_c^2 v_{rel,t} \tag{3.22}$$

where η is the viscous coefficient (-), typically set in the range between 0 and 0.1, which describes the resistance to slip (viscosity) of particle-particle contacts (MARTIN et al., 2009; MARTIN; BORDIA, 2009; WONISCH et al., 2007). Furthermore, grain growth is essentially hindered during fast sintering due to rapid heating rates (GARCÍA; KLEIN; HOTZA, 2012; GÓMEZ et al., 2016; WANG et al., 2020); thus, it was neglected in the present model.

3.2.4 Generation of numerical samples

The numerical sample was produced by randomly placing spherical particles with a diameter of 0.2 µm into a cylindrical volume. The random generation was carried out via the force-biased algorithm implemented in the MUSEN software (DOSTA et al., 2019; DOSTA; SKORYCH, 2020). Particles are iteratively rearranged to minimize interparticle forces, which are calculated as a function of their normal overlaps. The rearrangement ends when the maximum overlap between all contacting bodies is smaller than a threshold specified by the user. It allows the generation of more homogeneous and isotropic packings. However, a minimal initial connectivity between particles is obtained, which does not represent the actual microstructure of the ceramic compacts. Therefore, after the placement of the particles was completed, the particle overlaps were increased to generate realistic initial connectivity by scaling particle size up by 1.5% of their primary diameter. This led to a final particle size of 0.20 µm, an increment of maximum overlap to 1.48% of the final particle size, and an average initial packing density of 0.62.

3.2.4.1 Specification of the outer layer

The determination of particles belonging to the outer layer was done in two stages based on the particle positions. Firstly, the number of particles belonging to the outer layer $\mathrm{N_p^{outer}}$ was calculated. To conserve overall heat transfer from the environment to the specimen $\mathrm{N_p^{outer}}$ (Equation 3.23) was approximated as the ratio between packing surface area $\mathrm{A_{sample}}$ (cylindrical shape) and the projected surface area $\mathrm{A_p}$ of a particle (s. Equation 3.4):

$$N_p^{outer} = \frac{A_{sample}}{A_p} \tag{3.23}$$

A total of 72,600 particles were estimated as belonging to the outer layer, considering the particles and sample's dimensions presented in Table 1. In the second stage, the calculated number of particles was selected to define the outer layer. Two sets were composed of all the particles for the correct distribution of objects between the cylinder bases and side. The first included all particles sorted by their distance to the plane parallel to the base and intersecting the centre of the cylinder (XY plane). The second had all particles sorted by their distance to the central axis (Z). Then, from each set, particles were selected in an amount corresponding to the ratio of the side area and area of the base of the cylinder, taking explicitly into account that the two obtained sets may intersect.

The TMS algorithm is presented in Figure 3.3. In the first step, the initial interparticle overlap is taken as the plastic overlap representing the contact surface flattening. That allows avoiding any initial stresses in the material. Afterwards, at each time step, the interparticle contacts are initially detected, and subsequently, followed by calculations of conductive heat transfer. For the particles in the outer layer, the additional convective and radiative transfer is computed. For each particle-particle contact, an average temperature is calculated and used as a criterion to determine what type of contact models will be used. The modified Hertz-Mindlin contact model is applied if the average temperature is below the minimum sintering temperature (s. Equations 3.13 - 3.15). When the average contact temperature reaches values equal to or higher than the minimum sintering temperature, and if the max densification criterion is below its threshold, the sintering model (s. Equation. 3.19 - 3.22) is applied. Otherwise, if the temperature exceeds the minimum sintering temperature but the interparticle overlap is higher than the specific threshold, the repulsive force (s. Equations 3.16 – 3.18) is applied. The calculated forces and heat streams update particle properties such as positions, temperatures, and velocities. Finally, the simulation time is updated, and a new calculation iteration is started. The algorithm runs until the simulation end time is reached.

Figure 3.3: Schematic representation of the algorithm of the TMS model explicating the main steps.

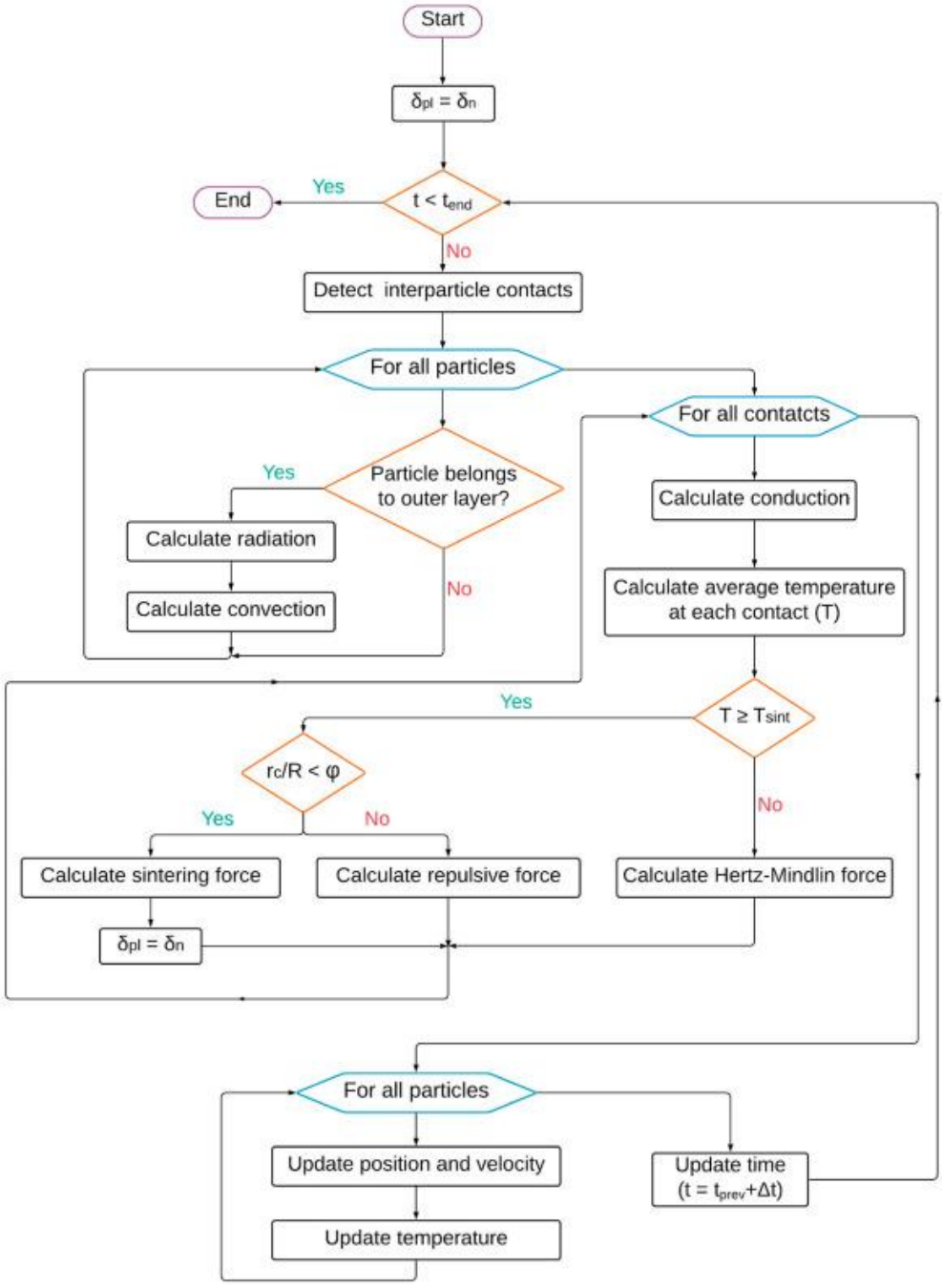

3.2.4.2 Scaling of mass and sample sizes

The size of the simulation time step directly influences the numerical stability of the solution (DOSTA et al., 2020; O'SULLIVAN; BRAY, 2004). As a means for speeding up DEM simulations, the mass of particles is often increased by several orders of magnitude, which allows increasing the simulation step (DOSTA et al., 2020;

HENRICH et al., 2007; IACOBELLIS; RADHI; BEHDINAN, 2019; MARTIN; BORDIA, 2009; MARTIN et al., 2014). Henrich and collaborators (HENRICH et al., 2007) have found that the scaling of particle mass S_{m_p} up to $8.6 \cdot 10^{-11} \frac{R^8}{\gamma_s \Delta_b}$ can be effectively used. Dosta et al. (DOSTA et al., 2020) applied a density scale factor of 10^{13}, which led to a condition $S_{m_p} < 4 \cdot 10^{-11} \frac{R^8}{\gamma_s \Delta_b}$. In the present study, the density was scaled by a factor of $1.8 \cdot 10^{19}$, which satisfies the described requirement. Considering the scaling of mass applied, the TMS model presented stability and convergence for time steps up to $1 \cdot 10^{-3}$ s.

Besides, the number of individual objects is a limiting factor for discrete element approaches (BURMAN; CUNDALL; STRACK, 1980; DOSTA et al., 2017, 2020; HENRICH et al., 2007; WONISCH et al., 2007). Thus, a limitation of about one million particles was imposed in the present work. Hence, the numerical packing was generated by scaling the experimental sample size down. Size correlations dependent on surface area and length were estimated by geometric derivations. Saving the proportions of experimental and numerical sample dimensions, a quadratic and a linear relationship of the diameters were obtained as the surface area a and length ℓ dependent size correlations:

$$a = \frac{d_{s,exp}^2}{d_{s,num}^2} \tag{3.24}$$

$$\ell = \frac{d_{s,exp}}{d_{s,num}} \tag{3.25}$$

To counterbalance the heat exchange given the mass and size scale, the scale parameters S_a and S_ℓ (Equations 3.26 – 3.27) were calculated by multiplying the size correlations (Equations. 3.24 – 3.25) by the particle mass ratio. By substituting $m = \rho V$ for the numerical and experimental geometries, a ratio between the densities multiplied by the size correlation and the volume ratio is obtained. Knowing that the volumes are functions of the respective cubic numerical and experimental diameters, they can be simplified to the diameter with the size correlations. Thus, S_a and S_ℓ assume the final linear and quadratic relationships with the diameters, respectively.

$$S_a = \frac{d_{s,exp}^2\, m_{num}}{d_{s,num}^2\, m_{exp}} = \frac{d_{s,exp}^2\, \rho_{num}\, V_{num}}{d_{s,num}^2\, \rho_{exp} V_{exp}} = \frac{d_{s,num}\, \rho_{num}}{d_{s,exp}\, \rho_{exp}} = \frac{d_{s,num}}{d_{s,exp}} S_{m_p} \quad (3.26)$$

$$S_\ell = \frac{d_{s,exp}\, m_{num}}{d_{s,num}\, m_{exp}} = \frac{d_{s,exp}\, \rho_{num}\, V_{num}}{d_{s,num}\, \rho_{exp} V_{exp}} = \frac{d_{s,num}^2\, \rho_{num}}{d_{s,exp}^2\, \rho_{exp}} = \frac{d_{s,num}^2}{d_{s,exp}^2} S_{m_p} \quad (3.27)$$

where $d_{s,exp}$ is the experimental sample diameter, $d_{s,num}$ is the numerical sample diameter, m_{exp} is the mass of Al_2O_3, m_{num} is the mass of numerical particles, ρ_{exp} is the Al_2O_3 density, ρ_{num} is the numerical particle density, V_{num} and V_{exp} are the respective numerical and experimental volumes.

The characteristics of the particles and the packing used here are presented in Table 3.1. A summary of all the parameters applied to the TMS model and their respective values are given in the Appendix.

Table 3.1: Features of the numerical particles and the packing.

	Parameters	Symbol	Unit	Value
Alumina particles	Diameter	d_p	mm	0.203
	Density of alumina	ρ_{exp}	kg/m^3	$3.95 \cdot 10^3$
	Young modulus	E	Pa	$3.8 \cdot 10^{11}$
	Atomic volume	Ω	m^3	$8.47 \cdot 10^{-30}$
	Surface energy	γ_s	J/m^2	1.1
	Grain boundary thickness times diffusion parameter	$\delta_b D_{0b}$	m^3/s	$1.3 \cdot 10^{-8}$
	Activation energy	Q_b	J/mol	$4.75 \cdot 10^5$
Packing features	Initial packing size (height ×diameter)		mm	22 ×22
	Average initial packing density	ρ_0	-	0.62
	Total number of particles	N^{tot}	-	1,157,970
	Number of particles in the outer layer	N_p^{outer}	-	72,600
	Maximum overlap	δ_{max}	mm	$3.01 \cdot 10^{-3}$
	Average overlap	$\bar{\delta}$	mm	$2.82 \cdot 10^{-3}$
	Total overlap	δ^{tot}	mm	9,556.88

3.3 RESULTS AND DISCUSSION

3.3.1 Heat transfer and thermal gradients

The fast heating of the numerical specimen before and during rapid sintering is presented in this section. Figure 3.4 reveals the profile of temperature evolution in the packing from room temperature to 1050 ºC over soaking time. The outer particles hit furnace temperature almost immediately – less than 10 s – owing to the high heat input by radiation and convection. Heat tended to build up near the outer surface at first.

Thus, the temperature in this region increased rapidly while the innermost layers of particles remained essentially at room temperature. Hence, the temperature gradient reached its maximum. Thermal radiation contributes to the heating of particles with the delta of the fourth power of the temperature of transmitting and receiving bodies $\left(\dot{Q}^{rad} \sim T_{env}^4 - T_{outer}^4\right)$. Therefore, it was indicated as the primary heating source when the cold sample was introduced into the hot furnace. Afterward, the transmission of heat particle by particle via thermal conduction promoted the raising temperature in the inner zone. With the properties and conditions applied, the numerical sample's core reached 48% of furnace temperature in 60 s, and 90% in 240 s. In 540 s – less than 10 min – the entire numerical sample arrived at furnace temperature, and the permanent regime was achieved.

Figure 3.4: Profile of temperature evolution over the soaking time at 1050°C of the numerical alumina sample initially at room temperature.

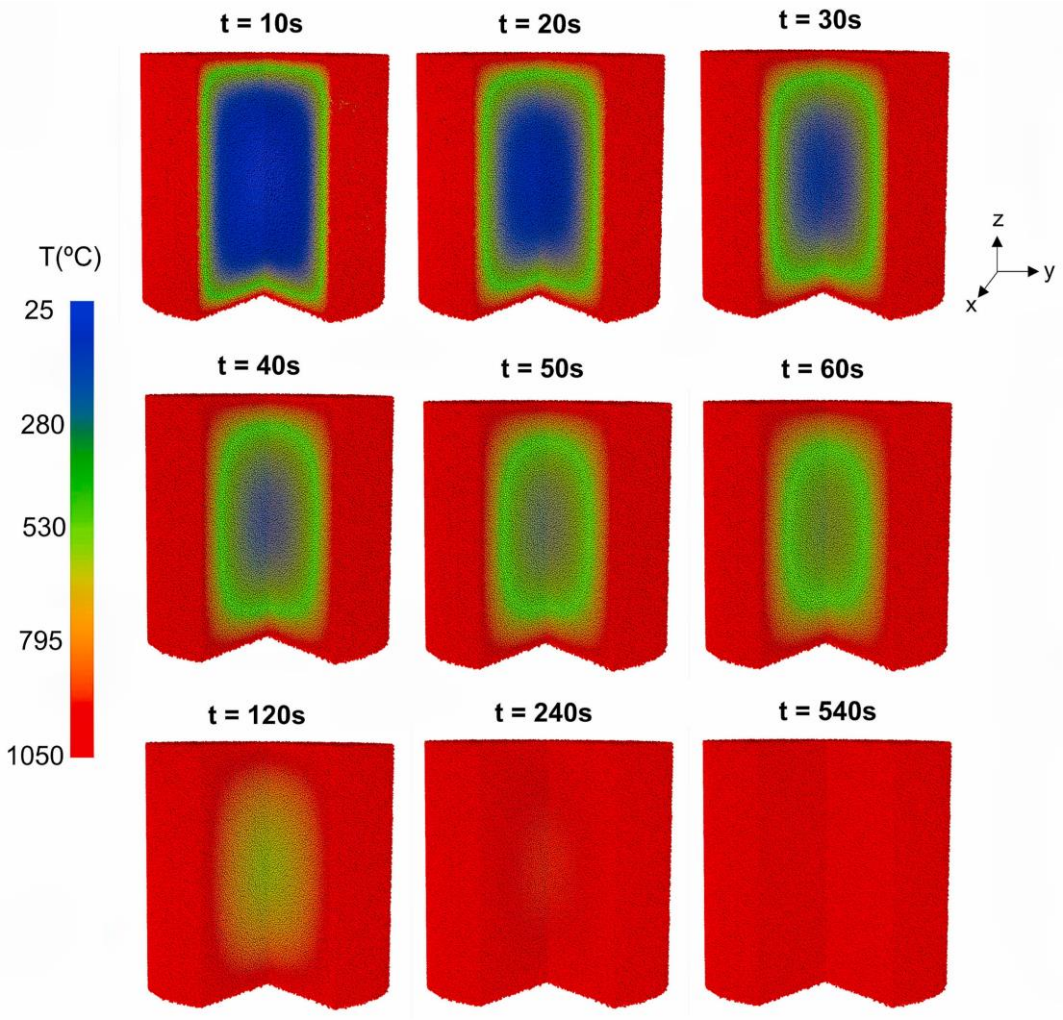

The temperature difference between the sample's surface (T_{outer}) and its center (T_{centre}) over time is shown in Figure 3.5(a) for both experimental and modeling data. A remarked initial steep thermal gradient was noted due to the low thermal diffusivity of the green Al_2O_3 body (GARCÍA; HOTZA; JANSSEN, 2011; POSSAMAI et al., 2012). Simulation results indicated temperature differences of up to 700 ºC after 60 s of soaking time, revealing high thermal gradients within the sample. In 240 s, the thermal difference was still over 145 ºC and decreased to less than 10 ºC after 540 min. A strong correlation and fitting were observed between the experimental and simulation results, as disclosed in Figure 3.5(b). A Pearson's R of 0.994 was obtained, expressing a remarkable degree of linear correlation. Besides, the regression equation explained 98.7% of the variation in the simulation result, demonstrating a good fit. The consistent agreement of the numerical and experimental results also reinforced that the thermal model parameters have been appropriately approximated. The statistic coefficients shown the potential of the TMS model in the description of thermal phenomena.

Figure 3.5:(a) Difference of temperature between furnace environment and sample's center (Tenv – Tcenter) over soaking time at 1050 ºC, and (b) correlation graph – comparison of numerical and experimental [16] results.

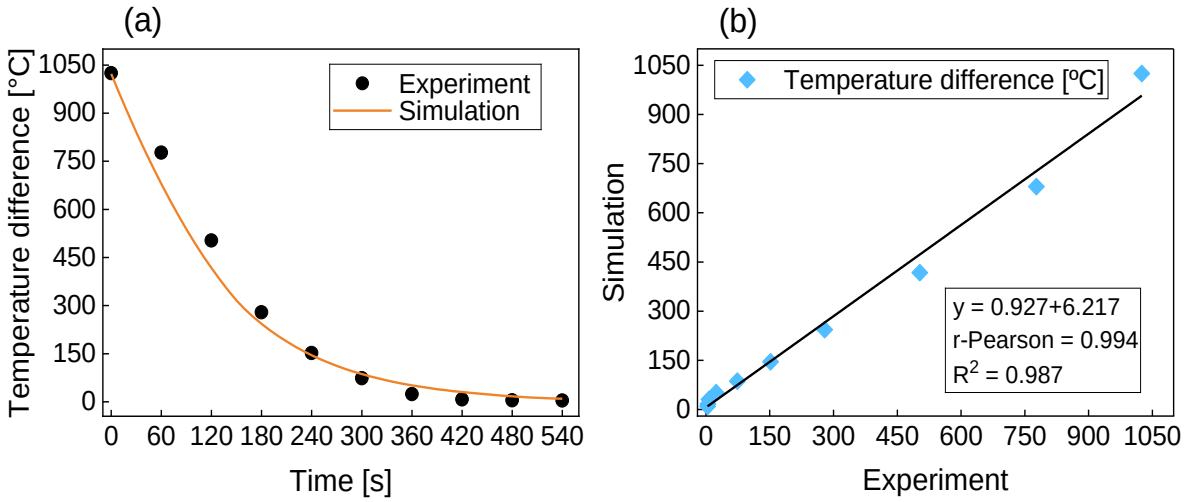

The simulation results of temperature distribution through the Al_2O_3 sample introduced in a pre-heated furnace at 1050 ºC, 1250 ºC, and 1350 ºC are presented in Figure 3.6. The temperature difference (y-axis) depicted the furnace temperature subtracted from the average temperature of a set of Al_2O_3 particles placed in equally sized spherical volumes homogeneously distributed along the radial direction of the

numerical sample. Zones near the external surface disclosed lower temperature differences with the furnace, whereas an increased thermal difference was observed moving toward the center. The sample's center, i.e., normalized distance = 0, required a considerable amount of time to achieve furnace temperature (temperature difference = 0). The temperature distribution indicated that heat dynamically transferred along the sample length from the outer shell toward its core. As a result, the inner particles did not experience the same thermal history as the outer particles most of the time. Hence, the non-isothermal behavior due to temperature gradients along the body was evidenced.

Figure 3.6: Progress of temperature profile as a function of sample's position in the radial direction over immersion time at 1050 ºC (dotted), 1250 ºC (dashed), and 1350 ºC (solid). The normalized distance equal to 0 corresponds to the average temperature at the center, whereas negative and positive values represent left- and right-hand sides, respectively.

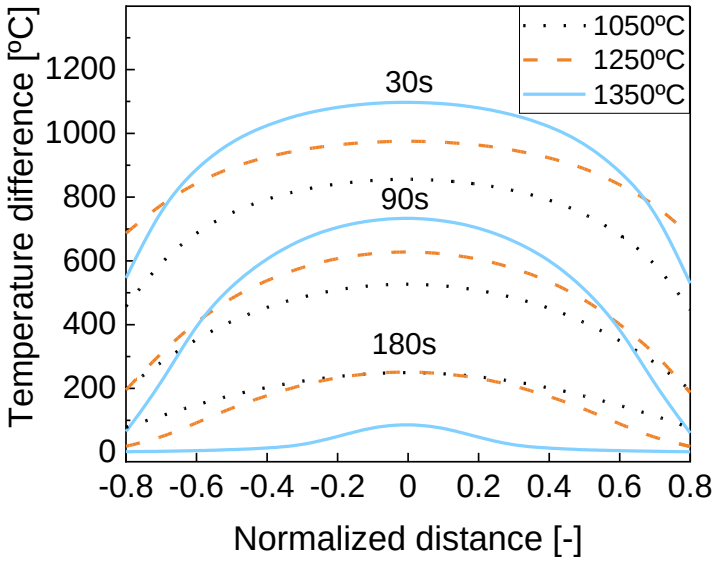

In regions closer to the center (normalized distances between -0.6 and 0.6), the sample sintered at 1350 ºC showed higher temperature gradients in the first 90 s, followed by the treatments at 1250 ºC and 1050 ºC, respectively. Sintering at 1350 ºC led to a maximum thermal gradient of ~1100 ºC in 30 s at the sample's center. This temperature difference dropped to 750 ºC after 90 s. For fast firing at 1250 °C, the temperature gradient reduced from ~1000 to 650 °C between 30 and 90 s. The lowest thermal gradients in this range were obtained for treatment at 1050 °C. This result

showed that the heating flux toward the lower temperature zones increases as the energy transferred to the compact is amplified, i.e., the higher the sintering/furnace temperature.

Furthermore, increasing the sintering temperature rises the densification of the green ceramic body by enhancing the diffusion process (BAE; BAIK, 1993; GILLIA; BOUVARD, 2000; JI et al., 2017; QING et al., 2018; WANG; CHEN, 2000). The progress of the densification implies an increase in the local thermal diffusivity leading to a synergistic effect on the heating rate (MOSKAL; MIKUŚKIEWICZ; JASIK, 2019). The boost in thermal diffusivity due to densification causes a substantial enhancement in the speed of heat propagation; therefore, the thermal gradients tend to disappear sooner (GARCÍA; KLEIN; HOTZA, 2012; POSSAMAI et al., 2012). The decreasing thermal gradient towards the external surface with time at 1350 ºC suggests an increasing thermal diffusivity of Al_2O_3 by the progress of densification from the outwards toward the interior. Treatment at 1050 ºC did not lead to densification since this temperature is not high enough to activate sintering mechanisms (GARCÍA; HOTZA; JANSSEN, 2011). Therefore, it took longer for thermal gradients to disappear when compared to treatments at 1250 and 1350 ºC.

3.3.2 Microstructure evolution and densification

3.3.2.1 Micro-macro densification

Numerically accessed microkinetic details can provide additional insights into microstructural development during the intermediate stage of rapid sintering. The evolution of the average coordination number (ACN) and r_c/R along the sample's radial length is disclosed in Figure 3.7.

Figure 3.7: Evolution of the (a) average coordination number (ACN) and (b) normalized contact radius (rc/R) over the normalized radial distance from the sample's center and dwell time for Al_2O_3 fast fired at 1250 and 1350 ºC.

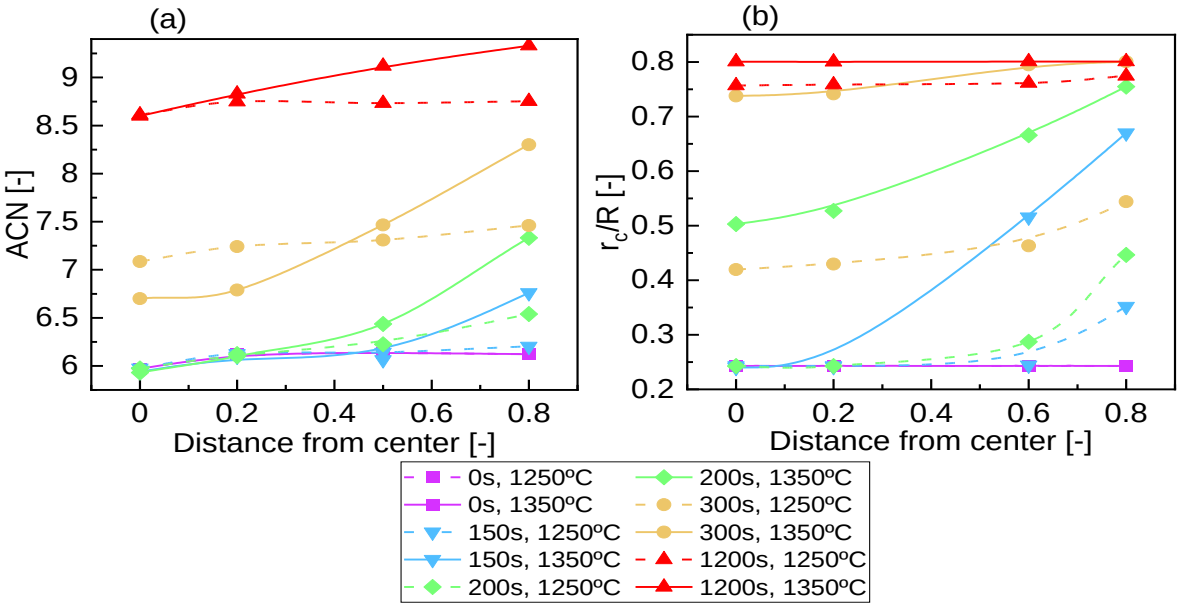

The ACN (Figure 3.7 (a)) was constant and equal to 6 along the initial sample. Exposure to the hot environment showed a noticeable increase within 150 s for fast firing at 1350 ºC, whereas it took between 150-300 s at 1250 ºC. The ACN in the most adjacent zone to the outer surface (distance = 0.8) increased from 6 to 8 in just 300 s, reaching 9 closest neighbors after 1200 s at 1350 ºC. In contrast, the coordination number remained at its initial value closer to the center (distance = 0.2) after 300 s. This demonstrated that the amount of heat propagated to the sample's core in the first 300 s was insufficient to cause significant microstructural changes in that region.

The coordination number of the sample sintered at 1250 °C, at a 0.8 normalized distance, increased by 1 unit after 300 s and reached approximately 9 at the end. A minor variation in ACN along the sample's length was observed when reducing the sintering temperature by 100 ºC.

The evolution of r_c/R over the sample's length (Figure 3.7 (b)) was notable from 150 s for both sintering temperatures. At this point, r_c/R essentially kept its initial value in the center, whereas an increase of 2.14 times occurred at a normalized distance of 0.8 at 1350 ºC. However, the r_c/R in the center increased by 2.1 times from 150 to 200 s. After 200 s, r_c/R presented a less accentuated gradient between the center and the surface.

For the Al_2O_3 particles sintered at 1250 ºC, no variation in r_c/R was observed at the center within the first 200 s. Nevertheless, at the distance of 0.8, there was a 2-fold increase over the same time interval. Significant differences in the center become noticeable only after 300 s.

In summary, the evolution of the coordination number and the r_c/R was not homogeneous throughout the ceramic packing; it rose from the outer surface toward the center during the intermediate sintering stage. Consequently, macroscale densification is expected to also show this trend, which can be attributed to thermal gradients under the non-isothermal conditions of fast firing. The steep increases of ACN and r_c/R in the zones closer to the outer surface suggest the formation of a densification front that tends to advance in the direction of the thermal gradients, that is, toward the compact interior, controlling further heat flux.

The macroscopic behavior of a ceramic body under fast sintering has its source at the sum of many microscopic interactions between powder particles. The micro-macro dependences were analyzed herein. The numerical results of the relative density over soaking time are shown in Figure 3.8(a). The graph considered the heating and sintering stages only. The y-axis outlined the overall bulk density increase within the ceramic body.

Figure 3.8: Numerical evolution of (a) relative density, (b) average coordination number (ACN), (c) densification rate over dwell time, and the (d) progress of the normalized average neck radius (r_c/R) over the temperature difference (bottom x-axis) and sintering time (upper x-axis) at 1250 ºC and 1350 ºC.

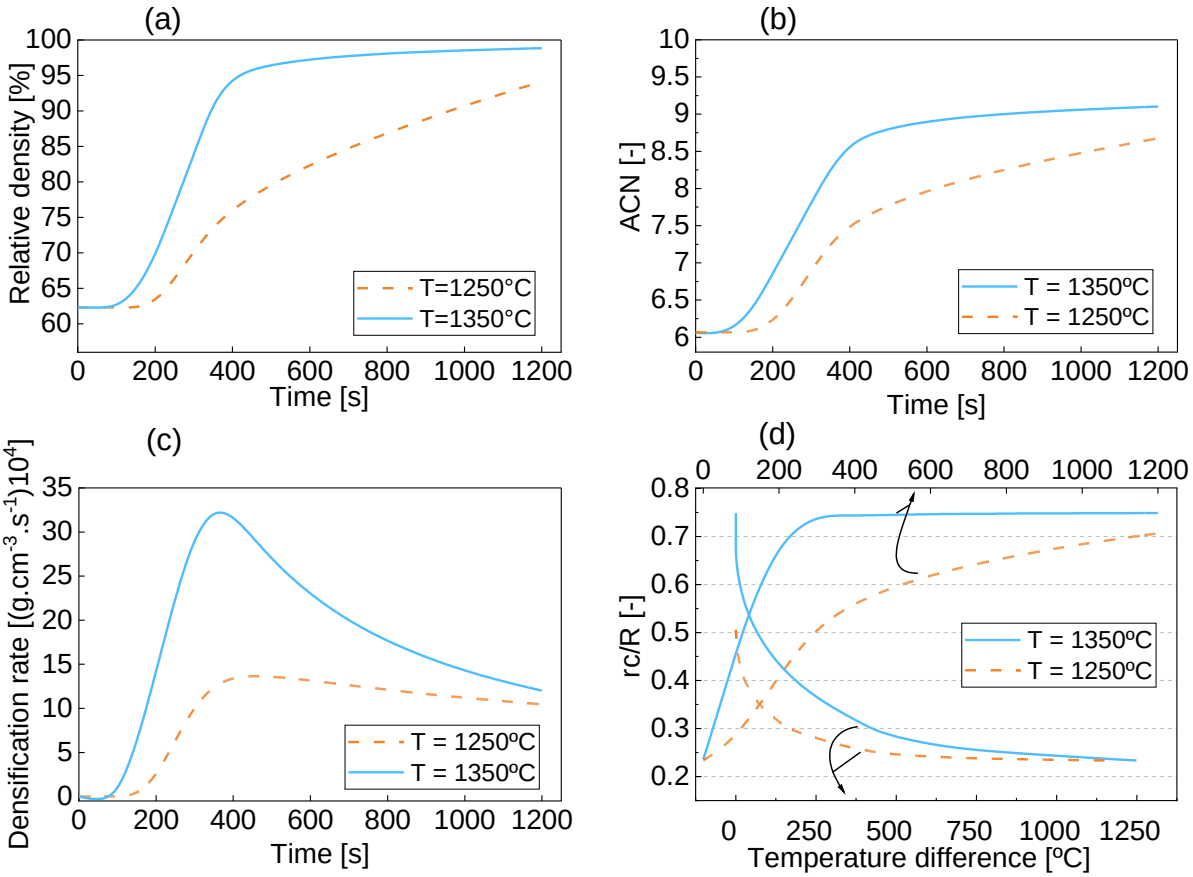

The increase in the relative density of the fast sintered sample at 1350°C began within ~100 s of treatment, whereas it took 150 s at 1250°C. The densification advanced rapidly, achieving 92% relative density in 350 s for fast-firing at 1350°C. Considering the same time interval, the fast-fired sample at 1250 ºC reached 73.5% of relative density. Following, a modest densification trend was observed at 1350 ºC until it reached 98.85% of maximum relative density in 1200 s. Although it progressed at a considerably lower rate than 1350°C, the treatment at 1250 ºC kept a moderate density increase, obtaining 94% of maximum relative density.

The coordination number results from the higher mobility of particles due to the higher sintering driving force [48,49], considering particles of equivalent size, shape, and mass. The steep increase in the relative density was also reflected in the fast increment of the ACN (Figure 3.8(b)). The rapid sintering procedure at 1350 ºC led to an increase in ACN of 1.4 times in the first 350 seconds, whereas an increment of 1.2 times was observed at 1250 ºC for the same time frame. Nevertheless, the ACN raised by 23% (350-1200 s) at 1250 ºC, whereas a modest increase above 13% was observed by increasing sintering temperature to 100 ºC. The lessening trend in the

dynamic growth rate of the ACN (Figure 3.8(b)) and densification (Figure 3.8(c)) after 350 s, especially at 1350 ºC, suggested that microstructural changes were reaching their maximum. This behavior has been identified experimentally as a 'frozen microstructure point' (L.WANG; SUN., 2020; WANG; CHEN, 2000) that ceramics might develop when the relative density reaches a certain point. The numerical results showed a frozen moment at ~ 92% of relative density, which is consistent with the experimental data of Wang and collaborators (L.WANG; SUN., 2020), in which the 'frozen microstructure point' was found at approximately 95% of relative density for pure sub-micrometric Al_2O_3, fast-fired by the direct-furnace-insertion procedure. On balance, an ACN of 1.5 and 1.4 times was achieved at the end for the fired samples at 1350 ºC and 1250 ºC, respectively.

Comparatively, a tendency to a sharp increase in the densification rate was registered within the first 350 s at both sintering temperatures, as indicated in Figure 3.8(c). The increment of 100 ºC at the sintering temperature intensified heat input into the particles, leading to an increase of almost 61% in the densification rate. Afterwards, the densification rate decreased for the sample sintered at 1350 ºC while it remained almost constant until the end of the treatment at 1250 ºC. At the endpoint (1200 s), the difference between the densification rates of sintering at 1350 and 1250 ºC was just 13%.

The progress of the normalized average neck radius r_c/R of the overall particles over the temperature difference and the sintering time is presented in Figure 3.8(d). A 3-fold increase in r_c/R accompanying the temperature gradient regime was observed from 1250 ºC to approximately 0 ºC in the first 200 s for fast sintering at 1350 ºC. The sample sintered at 1250 ºC experienced an increase of only 1.75 times in r_c/R for the same time interval, which indicates that the decrease in sintering temperature leads to a delay of 50% in densification within the first 200 s. Besides, it was observed that the sample fired at 1250 ºC remained under thermal gradients for 100 seconds longer. Thus, increasing the sintering temperature enhances the densification rate and the speed at which temperature gradients pass throughout the sample.

3.3.2.2 Microstructural effects of temperature gradients

Experimental studies point to a characteristic densification behavior of fast firing (CAMM, 2017; GARCÍA et al., 1995; GHORRA, 2008) in which a denser shell is formed in the sample surface and moves inwards. The simulation results foresaw this characteristic microstructure owing to forming a densification front in the intermediate stage of fast firing at 1350 ºC, as shown in Figure 3.9. A denser outer layer of particles was formed and enveloped the porous inner region (Figure 3.9(a)). The highlighted region of the simulation image nicely corresponds to the micrography (Figure 3.9(b)) obtained experimentally by García and collaborators (GARCÍA; HOTZA; JANSSEN, 2011). The densification front is the product of thermal gradients generated by the rapid heat input and is pointed as the controller agent of the heat flow within the compact. Thus, forming a dense layer of Al_2O_3 at the interface between the furnace environment and the green sample significantly affects the temperature profile distribution. High densification rates observed during fast sintering seem to be related to a change in the sample's internal structure, which is not considered a complementary sintering mechanism but can contribute to the improvement of sintering (GARCÍA; HOTZA; JANSSEN, 2011).

Figure 3.9: Visualization of the densification front from (a) the numerical sample by the TMS model and (b) SEM image of a cross-section of fast-fired Al_2O_3, showing the densification front moving from the dense outer surface D toward the porous center of the sample P (GARCÍA; HOTZA; JANSSEN, 2011) (with copyright permission from the journal). The numerical representation is a half-section in the y-axis of the cylindrical sample, with a thickness of 2 layers of particles at 550 s and fast-fired at 1350 ºC.

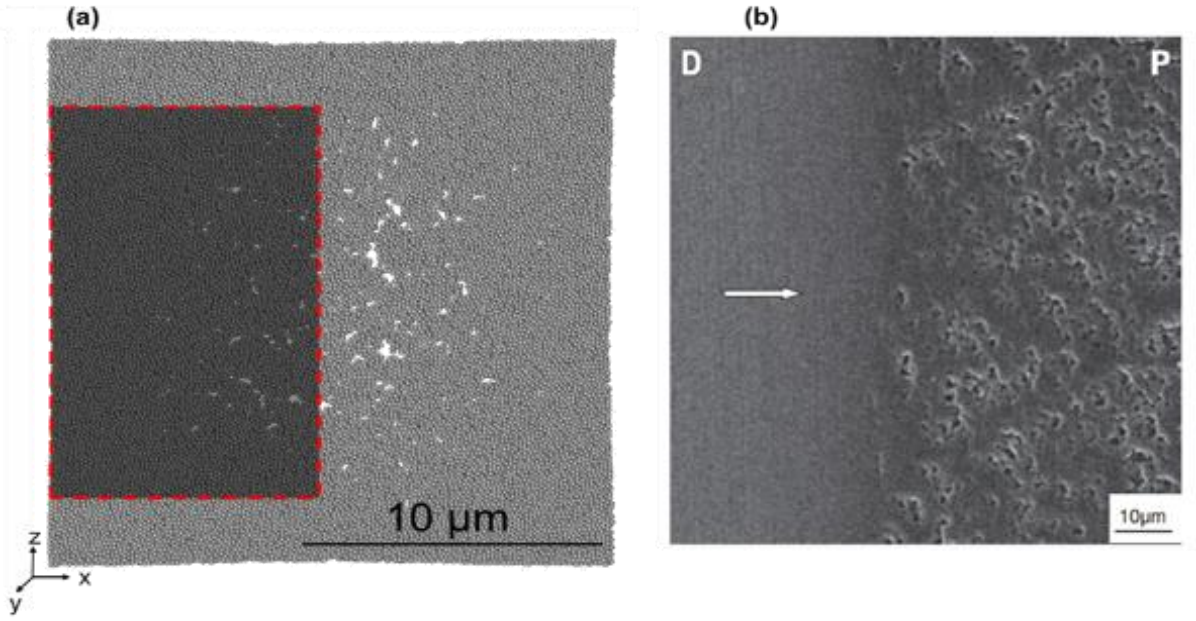

3.2.2.3 Radial Shrinkage

The radial shrinkage of the simulation samples sintered at 1250 ºC and 1350 ºC is shown in Figure 3.10. The initial stage, 250 s, 350 s, and the last simulation time point are illustrated. The radial shrinkage S_r was defined by Equation 3.27 as a function of the cross-section diameter of the cylindrical sample at the beginning $D_{t=0}$ and after each specified time interval $D_{t=x}$.

$$S_r = \frac{D_{t=0} - D_{t=x}}{D_{t=0}} \tag{3.27}$$

A radial shrinkage of 10% accompanied the increment in the density after 250 s of fast firing at 1350 ºC, while this value is 2.2 times smaller when 100 ºC decreased the sintering temperature. At 350 s, the radial shrinkage progressed to 13.6% and 7.8%

for fast sintering at 1350 ºC and 1250 ºC, respectively. After 1200 s, the TMS model forecasted 15.4% of radial shrinkage for the Al_2O_3 body fast fired at 1350 ºC and 14.5% for sintering at 1250 ºC. The foretold values for the radial shrinkage agree with the micro-macro densification features discussed beforehand. Furthermore, the shrinkage values predicted by the present method agree with previous experimental work (SOMTON et al., 2020; TATAMI et al., 2006).

Figure 3.10: Visualization of cross-sections of 3D simulation in initial (t = 0s), intermediate (t = 250s, t = 350s) and end-stage (t = 1200s) for the Al_2O_3 samples fast-fired at 1250 ºC and 1350 ºC. The cross-section view represents the circular section of the cylindrical sample cut in half of its height (z-axis).

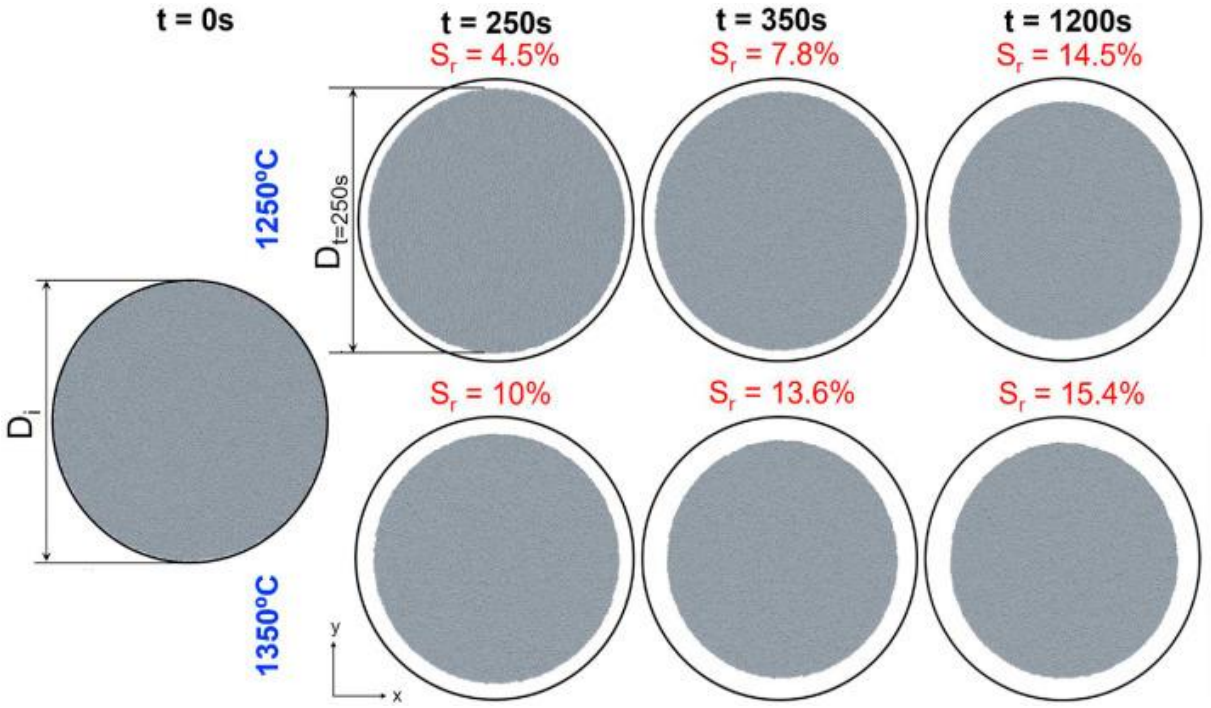

3.2.2.4 Influence of sintering parameters on microstructural evolution of defects

Randomly distributed mesoscopic defects were artificially introduced by deleting particles inside the initial Al_2O_3 sample with the scope of further analysis of the microstructure development. The defects were created in spherical-shaped regions (purple coloured), simulating a sort of internal mesopores. The defects evolution in the final microstructures after sintering at 1350 ºC with instantaneous heating rate, 250 ºC/s, and 10 ºC/min, in contrast with fast firing at 1250 ºC, is depicted in Figure 3.11.

Figure 3.11: Microstructural evolution of defects after sintering at different temperatures and heating rates. The pristine sample represents the initial microstructure, and the following images refer to each treatment's endpoint. The defects are purple colored at the initial condition and cyan after each treatment. The numerical representation is a half-section view in the y-axis of the cylindrical sample with 2 layers of particles thickness.

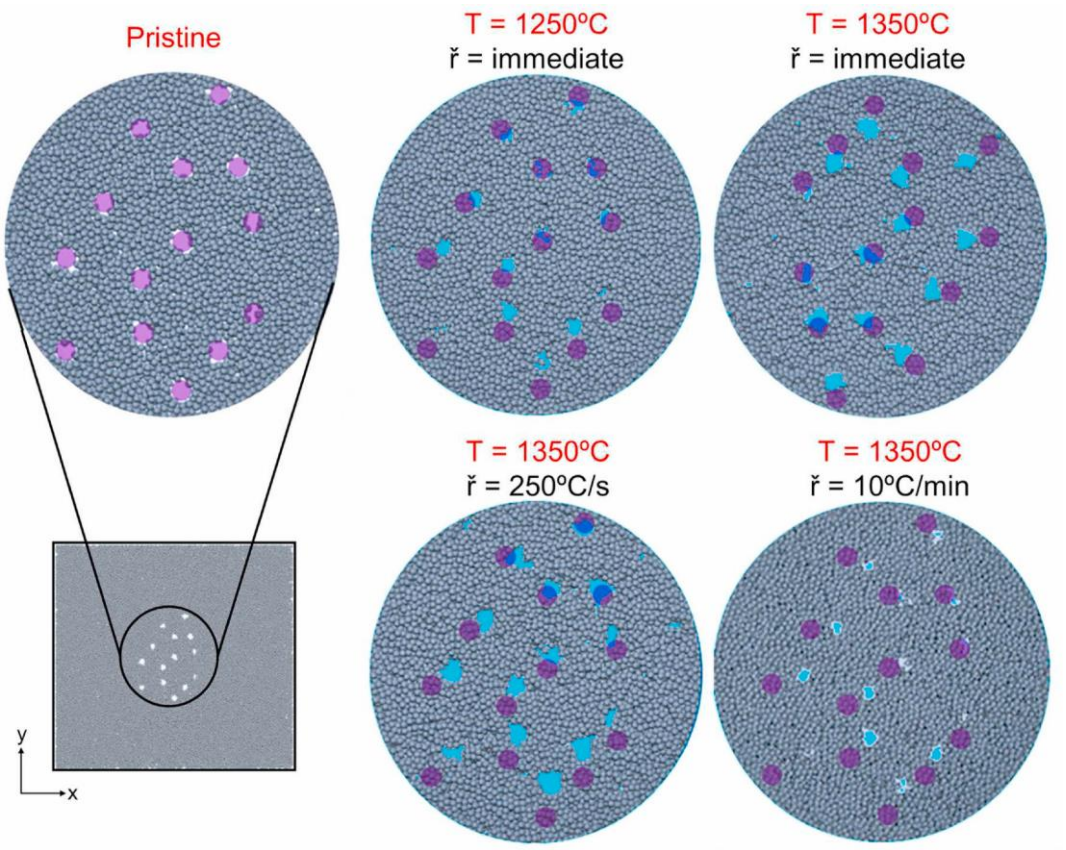

Compared to the pristine sample, the morphology of the defects did not present considerable dissimilarity between the high heating rates (instantaneous and 250 ºC/s) modelled under fast firing at 1350 ºC. However, an essential microstructural evolution with a definite trend to the closure of internal defects was observed by applying a conventional firing protocol (Ř = 10 ºC/min) at 1350 ºC. Decreasing sintering temperature by 100 ºC (T_{sint} = 1250 ºC) and keeping the instantaneous heating rate, a substantial reduction in the size of the defects was observed, which led to a significant morphological variation in defects with a tendency to obtaining a denser sample.

The antagonistic effect of temperatures and heating rates on the significant evolution of defects under rapid firing may have originated, among other factors, in the fast spread of heat due to high thermal gradients. The abrupt propagation of heat did

not provide enough time for the activation of specific mechanisms that might have favoured mass transfer and the relief of stresses trapped in the region of the defects. Therefore, the higher temperature did not lead to a significant evolution of the defects under rapid firing, which may have originated in the rapid spread of heat due to the high thermal gradients.

3.4 CONCLUSION AN OUTLOOK

An original model for thermomechanics coupled with sintering (TMS) was formulated and implemented in the DEM simulation framework MUSEN. Incorporating heat transfer concepts, transient temperature regimes, and sintering allowed the representation of fast sintering kinetics. The TMS model provided new insights into microscale features that contribute to the macro behavior of ceramics under rapid firing.

The simulation results showed relevant details of the densification process concerning sintering temperature thermal and density gradients, including the evolution of micro-kinetics, named the coordination number and the distribution of the cohesive neck size, and the progress of defects. The TMS model agreed well with experimental data of thermal gradients in the range analyzed. The numerical heating profiles showed that the outer surface reached furnace temperature almost immediately. Afterwards, the heat flowed particle by particle toward the sample’s core. The densification did not occur homogeneously according to the micro-kinetics investigation over the sample’s length, and the density gradients tended to be accentuated for higher sintering temperatures. The densification front phenomenon was also foreseen.

The increment in the neck radius and coordination number from the outer layer to the centre of the sample confirmed the densification path during the fast-firing procedure. The interplay of the microscopic phenomena led to the increase in the overall relative density and shrinkage. Although the increase in sintering temperature has positively affected the relative density, densification rate, and coordination number, higher sintering temperatures did not necessarily represent the best condition for internal defect retrenchment. Indeed, an opposite effect was observed — the substantial enhancement in the speed of heat propagation that caused the thermal gradients to disappear sooner.

The proposed TMS model allows analyzing and predicting microscale phenomena during fast sintering, which are not trivial to be obtained experimentally. This model has a high potential to be applied in other systems, including incorporating other mechanisms for rearrangement and densification, such as viscous flow.

CHAPTER 4 – SIMULATION OF FAST-FIRING DENSIFICATION BY THE DISCRETE ELEMENT METHOD[2]

4.1 INTRODUCTION

The sintering process is a critical step in the microstructural evolution of components produced by powder technology, in which a dispersed state of matter is transformed into a body with higher density (TEIXEIRA et al., 2021). Since its first publication a couple of decades back, fast sintering approaches have attracted significant scientific and technological interest for enabling enhanced productivity by obtaining highly dense fine-grained goods in short periods, which implies shorter production times, lower energy consumption per payload, lowered labor costs, and improved product reliability (GHORRA, 2008; SINGH; SUBRAHMANYAM, 1976).

Experimental studies on fast firing applied to ceramic systems are widely found in the literature (GERMAN, 2010; SINGH; SUBRAHMANYAM, 1976). However, pure experimental methodologies can be time-consuming and do not allow the identification of sintering behavior contributing to the final product quality (ALVES et al., 2021). Notwithstanding, García and collaborators (GARCÍA; HOTZA; JANSSEN, 2011) have addressed an essential contribution by experimentally assessing in-situ thermal gradients through a rapid-fired Al_2O_3 body. However, experimental limitations restricted such analysis to low temperatures. In this context, modelling and simulation approaches have clarified physical, chemical, and thermal phenomena (CHEN et al., 2019), leading to the control and optimization of processing techniques and material properties. Despite considerable numerical explorations on the sintering (MARTIN et al., 2016b), a few works approach the numerical modeling of fast firing (POSSAMAI et al., 2012). Still, unrealistic assumptions have been supposed, such as considering the green ceramic as a non-porous body and the absence of shrinkage during the densification. Hence, understanding the microscale features of the densification process associated with heat transfer phenomena during fast firing is still a vast investigation area.

Herein, macro and microscale details of densification under non-isothermal sintering are explored using numerical simulations to forecast microstructural

[2] Published in Open Ceramics https://doi.org/10.1016/j.oceram.2023.100516

phenomena. We integrated heat transfer concepts, transient temperature regime, and sintering/contact forces to build a DEM model and applied it to an Al_2O_3-based ceramic. The paper's scope includes model validation with experiments. Emphasis is addressed on the evolution of thermal and densification gradients over temperature and along the sample's length. Numerical validation has demonstrated good thermal behavior representation of the fast-sintered Al_2O_3 specimen. Finally, macro-micromechanical analyses of time-dependent microstructure evolution in terms of the relative density and the distribution of the cohesive neck size are presented.

4.2 EXPERIMENTAL

4.2.1 Problem design

The numerical sample was generated by randomly placing spherical particles with a diameter of 0.2 μm into a cylindrical volume. The packing was designed to preserve particle size and scaled the dimensions of the Al_2O_3 compact down due to computational limitations. A transient heating process was assumed to determine the temperature field inside the numerical packing. The particles were grouped into two zones based on their position to consider the different heat transfer mechanisms: the outer layer, where convection, radiation, and conduction mechanisms are engaged, and the inner zone, where only interparticle conductive heat transfer occurs. Simulation samples were heated from 25 to 1050 and 1350°C. An instantaneous heating rate was applied to resemble the direct introduction of the sample into a furnace at a sintering temperature. The furnace was only modelled by the boundary conditions applied to the body surface. Its temperature was assumed to remain constant over the process, and heat losses between the sample and the enclosed environment were neglected. A half-section view of the numerical sample, highlighting the outer and the inner layers and the heat transfer mechanisms, is illustrated in Figure 4.1.

Figure 4.1: Half-section view of the 3D simulation sample highlighting the outer layer and the inner zone, along with an illustration of the heat transfer mechanisms considered in the model.

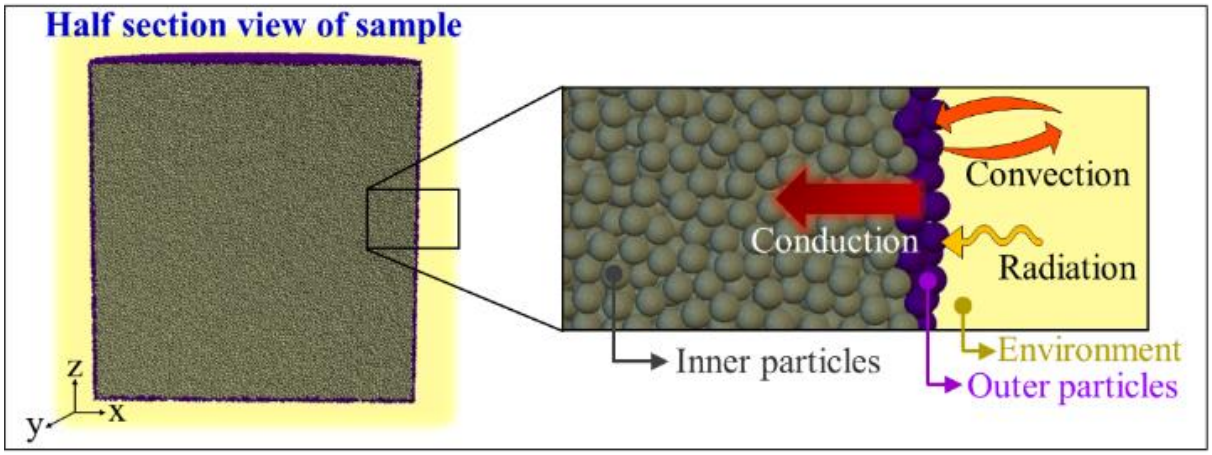

4.2.2 Modeling approach

The thermo-mechanics coupled with the sintering model was developed to account for thermal gradients typically present during rapid sintering. The heat transfer mechanisms considered to provide significant contributions were:

- Radiation – emitted by the surroundings, which corresponds to the furnace environment, and absorbed on particles at the sample surface;
- Convection – between the stagnant air inside the furnace and particles on the sample surface and
- Conduction – pair-wise heat transfers between contacting particles.

Equation 4.1 presents the explicit calculation of each heat transfer mechanism. The particles were assumed to be opaque grey emitting spherical bodies with identical chemical compositions. Only thermal energy was transferred. Heat production or consumption due to chemical reactions and thermal expansion were neglected.

$$\begin{cases} \boldsymbol{Radiation} \\ Q^{rad} = \varepsilon\,\sigma\,A_p\,S_a(T_{env}^4 - T_{outer}^4) \\ A_p = \pi\,R^2 \\ \boldsymbol{Convection} \\ Q^{conv} = A_p\,S_a\,h_c(T_{env} - T_{outer}) \\ \boldsymbol{Conduction} \\ Q^{cond} = 2\,r_c \cdot S_\ell \cdot f_{res}(\delta_n) \cdot \kappa(T) \cdot (T_j - T_i) \\ r_c = \sqrt{2\,R\,\delta_n} \\ \delta_n = R_i + R_j - |\vec{X}_i - \vec{X}_j| \\ \kappa(T) = 5.85 + \dfrac{15360\,e^{-0.002\,T}}{T + 516} \end{cases} \tag{4.1}$$

where Q^{rad} is the heat transfer rate by radiation (W); ε is the surface emissivity (dimensionless); σ is the Stefan-Boltzmann constant (W/m^2·K^4); A_p representative contact area (m^2) (GANERIWALA; ZOHDI, 2016); S_a is the parameter of scaling for mass-surface-dependent heat transfer (dimensionless); T_{env} is the environment temperature (K); T_{outer} is the outer particle temperature (K); R is the particle radius (m); Q^{conv} is the heat transfer rate by convection (W); h_c is the convective heat transfer coefficient (W/m^2.K); Q^{cond} is the heat transfer rate by convection (W); r_c is Coble's contact radius (m) (COBLE, 1958); δ_n is the normal overlap (m); X is the particle position (m); S_ℓ is a scaling parameter for mass-length-dependent heat transfer of the particles (dimensionless); $f_{res}(\delta_n)$ is the thermal conduction resistivity factor (dimensionless); $\kappa(T)$ is the temperature-dependent thermal conductivity (W/m·K); T_i and T_j are the temperatures (K) of particles. The subscript n represents the normal direction; i and j, two neighboring particles. The subscript n represents the normal direction; i and j, two neighboring particles.

The heat transferred to a single particle was expressed as the sum of each thermal exchange experienced. Thus, the energy conservation equation for every particle at each time step was calculated by Equation 4.2

$$\begin{aligned} m_p c_p(T)\frac{dT}{dt} &= Q^{rad} + Q^{conv} + \sum Q^{cond} \\ c_p(T) &= 1117 + 0.14\,T - 411\,e^{-0.006\,T} \end{aligned} \tag{4.2}$$

where m_p (kg) is the particle mass and $c_p(T)$ is the temperature-dependent specific heat capacity (J/kg K).

Particle-particle interactions were modeled by either the non-isothermal sintering model, the modified Hertz-Mindlin, or the repulsive force contact models depending on the average temperature of contacting particles and the normalized neck radius. García et al. (GARCÍA; HOTZA; JANSSEN, 2011) found that powder compacts of ~0.2 µm alumina particles showed no evidence of significant dimensional changes up to 1050 ºC, i.e., sintering mechanisms seemed to be still inactive up to this temperature. Hence, this temperature threshold was implemented as a minimum temperature below which no sintering occurs. Moreover, exploratory simulations confirmed that fully dense packing was achieved at $r_c/R = 0.8$. It is important to remark that r_c/R is a microscale densification parameter independent of material type or packing size. A schematic illustration of r_c and R is shown in Figure 4.2.

Figure 4.2: Illustration of two particles overlapping showing the radius R and contact radius r_c.

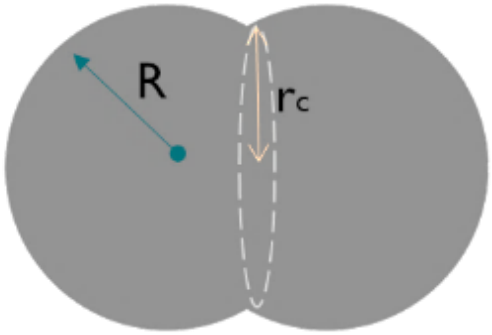

The application of each contact model according to the specified conditions is expressed by Equation 4.3:

$$
\begin{cases}
\textbf{\textit{Hertz}} - \textbf{\textit{Mindlin}} & \\
\overline{\mathrm{T}} < 1050^{\circ}C & \mathrm{F_n^{HM}} = \mathrm{K_n}\delta_\mathrm{n}^{\mathrm{HM}} - \mathrm{B_n}\mathrm{v_{rel,n}} \\
& \mathrm{F_t^{HM}} = \mathrm{K_t}\delta_t - \mathrm{B_t}\mathrm{v_{rel,t}} \\
& \delta_\mathrm{n}^{\mathrm{HM}} = \delta_\mathrm{n} - \ \delta_\mathrm{pl} \\
& \delta_\mathrm{pl} = \mathrm{R_i} + \mathrm{R_j} - |\vec{\mathrm{X}}_\mathrm{i}(\mathrm{t}_0) - \vec{\mathrm{X}}_\mathrm{j}(\mathrm{t}_0)| \\
\textbf{\textit{Sintering forces}} & \\
\overline{\mathrm{T}} \geq 1050^{\circ}C \text{ and } \dfrac{\mathrm{r_c}}{\mathrm{R}} \leq 0.8 & \Delta_\mathrm{b} = \dfrac{\Omega}{\kappa_\mathrm{B}\overline{\mathrm{T}}}\delta_\mathrm{b}\mathrm{D_{0b}}\,\mathrm{e}^{\frac{-\mathrm{Q_b}}{\mathrm{R_g}\overline{\mathrm{T}}}} \\
& \mathrm{F_n^{sint}} = \dfrac{\alpha}{\beta}\pi\ \mathrm{R}\,\gamma_\mathrm{s} - \dfrac{\pi}{2\,\beta\Delta_\mathrm{b}}\mathrm{r_c^4}\,\mathrm{v_{rel,n}} \\
& \mathrm{F_t^{sint}} = -\,\eta\dfrac{\pi\,\mathrm{R}}{\beta\Delta_\mathrm{b}}\mathrm{r_c^2}\,\mathrm{v_{rel,t}} \\
\textbf{\textit{Repulsive force}} & \\
\overline{\mathrm{T}} \geq 1050\ ^{\circ}\mathrm{C} \text{ and } \dfrac{\mathrm{r_c}}{\mathrm{R}} > 0.8 & \mathrm{F_n^{rep}} = \mathrm{K_n}\delta_\mathrm{n}^{\mathrm{rep}} - \mathrm{B_n}\mathrm{v_{rel,n}} \\
& \delta_\mathrm{n}^{\mathrm{rep}} = \delta_\mathrm{n} - \delta_\mathrm{max}
\end{cases}
\tag{4.3}
$$

where $\mathrm{F^{HM}}$ is the Hertz-Mindlin contact force (N); K is the elastic stiffness; B is the viscous damping; $\delta_\mathrm{n}^{\mathrm{HM}}$ is the Hertz-Mindlin modified interparticle overlap (m) in the normal direction; δ_pl is the plastic" overlap (m); $\mathrm{v_{rel}}$ is the relative velocity (m/s), Δ_b is the mass transfer parameter ($m^4 \cdot s/kg$); Ω is the atomic volume (m^3); κ_B is the Boltzmann constant ($m^2 \cdot kg/K \cdot s^2$); δ_b is the grain boundary thickness (m); $\mathrm{D_{0b}}$ is the diffusion coefficient (m^2/s); $\mathrm{Q_b}$ is the activation energy (J/mol); $\mathrm{R_g}$ is the universal gas constant (J/K·mol); $\mathrm{F^{sint}}$ is the sintering force; α and β are model parameters (dimensionless) related to the dominant mass transport mechanism; γ_s is the surface energy of particles (J/m^2); η is the viscous coefficient (dimensionless); $\mathrm{F^{rep}}$ is the repulsive force (N); $\delta_\mathrm{n}^{\mathrm{rep}}$ is the repulsive overlap (m); and δ_max is the maximal interparticle overlap (m) in the fully densified state (80% of particle radius). The subscript t represents the tangential direction.

The numerical model was implemented in DEM using the open-source software MUSEN (DOSTA; SKORYCH, 2020). A summary of the simulation parameters is presented in Table 4.1.

Table 4.1: Summary of simulation parameters.

Parameters	Symbol	Unit	Value
Convective heat transfer (BERGMAN; LAVINE, 2017)	h_c	$W/m^2 \cdot K$	5
Surface emissivity (BERGMAN; LAVINE, 2017)	ε	-	0.8
Thermal conduction resistivity factor (TEIXEIRA et al., 2021)	f_{res}	-	0.18
Factor of size scaling for surface dependency (TEIXEIRA et al., 2021)		-	$1.1 \cdot 10^{-3}$
Factor of size scaling for length dependency (TEIXEIRA et al., 2021)	S_ℓ	-	$1.21 \cdot 10^{-6}$
Slip parameter (MARTIN et al., 2009)	η	-	0.01
Sintering model parameters (MARTIN et al., 2009)	α, β	-	4, 4.5
Simulation time step (TEIXEIRA et al., 2021)	Δt	s	0.001

4.3 RESULTS AND DISCUSSION

The experimental points (red-filled dots) and the simulation curve (black continuous line) of relative density over time for sintering at 1350 ºC are presented in Figure 4.3(a). The evolution of relative density in the simulation sample closely matches the experimental one. The correlation analysis shows a coefficient of determination r^2=0.99 and a Pearson's coefficient of correlation r=0.99, which indicates that the DEM model accurately describes the macro densification phenomena within the evaluated range.

Figure 4.3: Evolution of (a) relative density and (b) sintering kinetics transition over time for Al_2O_3 fast fired at 1350 ºC.

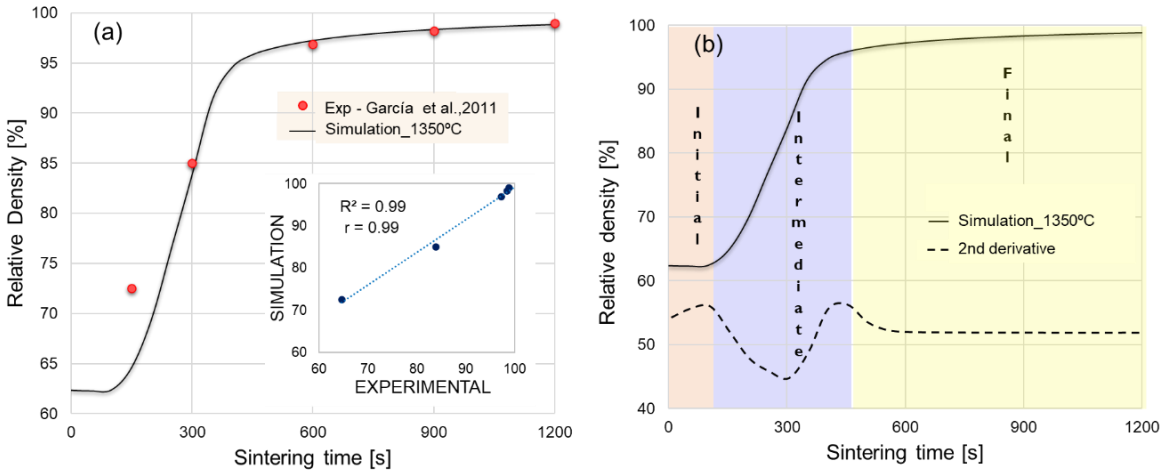

According to the second-order derivative of the densification curve, the kinetics transition (as depicted in Figure 4.3(b)) displays three primary stages of sintering. The first stage, involving the formation of necks, endures only 100 s due to the rapid heating of outer particles upon exposure to the sintering temperature and moderate initial packing density. Densification then advances quickly, achieving almost 96% relative density within 433 s. Finally, it attains a steadily increasement from 600 s to 1200 s.

In rapid sintering approaches, temperature gradients may cause gradients on microscale densification. Hence, micro-localized density increments over the sample's length are investigated, using the normalized neck radius r_c/R as the micro-densification parameter, as shown in Figure 4.4. The evolution of r_c/R over the sample's size was notable from 150 s. At this time point, r_c/R practically kept the initial value (0.24) in the sample's center (normalized distance = 0), whereas it reached 0.67 at a normalized length of 0.8. However, between 150 s and 200 s, r_c/R fast advanced from 0.24 to 0.5 in the center, indicating that densification was activated in the sample's core. After 300 s, a less accentuated r_c/R gradient was observed over the sample's length until the whole body reached 0.8. The steep increases in r_c/R in the zones closer to the outer surface suggest the formation of a densification front that tends to advance in the direction of the thermal gradients, that is, toward the sample's interior.

Figure 4.4: Microscale densification accounted for the evolution of the normalized neck radius (r_c/R) over the normalized radial distance from the sample's center and soaking time for Al_2O_3 fast fired at 1350 ºC. The normalized distance equal to 0

corresponds to the average temperature at the sample's centre whereas the positive values represent the distance from the centre on the right-hand side.

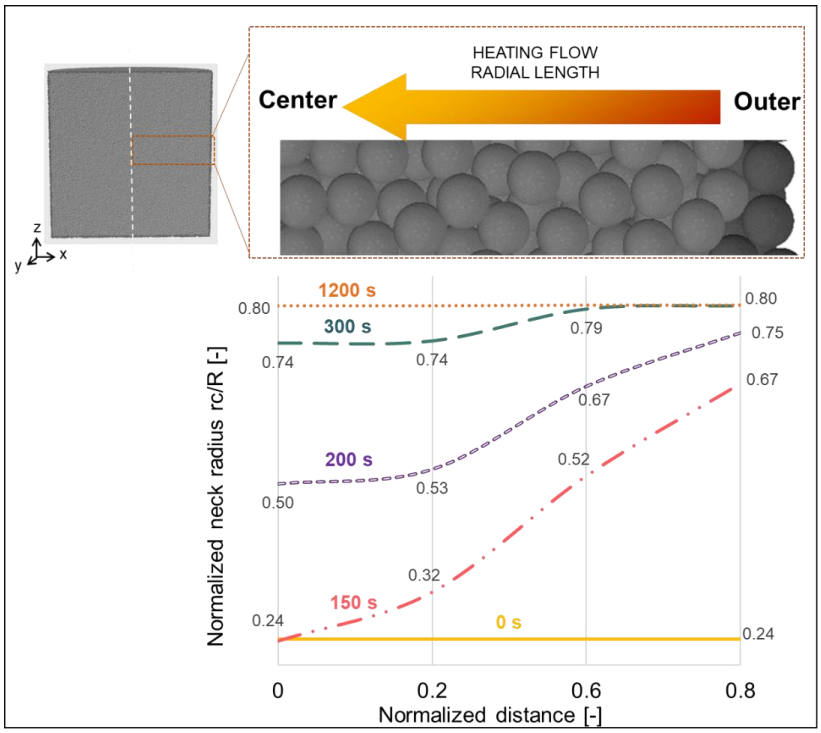

Figure 4.5 displays the temperature difference between the outer layer (T_{outer}) and center (T_{center}) over time for experimental and simulated data. The curves of the simulation and experiment closely match and reveal high thermal gradients within the sample. Notably, temperature disparities of roughly 500 ºC are observed within the sample within just 120 s, with a thermal difference of over 145ºC remaining after 240 s. These gradients result from the low thermal diffusivity of the green Al_2O_3 body (GARCÍA; HOTZA; JANSSEN, 2011; POSSAMAI et al., 2012). After 540 s, the difference decreased to less than 10 ºC. Additionally, the inset graph shows the correlation parameters between the experimental and simulation, with a Pearson's r=0.99 indicating an excellent linear correlation. The regression equation, r^2=98%, demonstrates good fitting. Thus, the statistical coefficients showcase the model's potential to describe thermal phenomena accurately.

Figure 4.5: Numerical and experimental temperature difference between the sample's surface and its center ($T_{outer} - T_{center}$) over a soaking time at 1050 ºC, and the correlation between simulation and experimental result (inset graph).

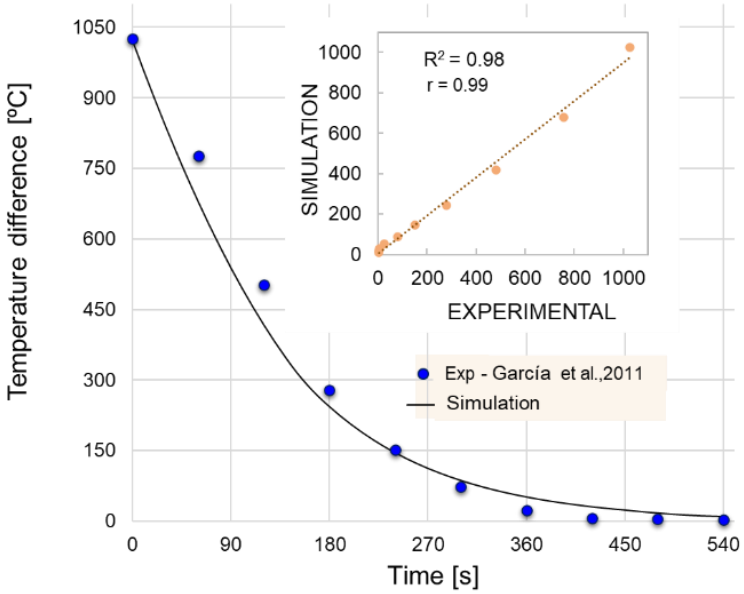

Figure 4.6 presents the temperature distribution in the simulation sample, which was rapidly heated at 1050 and 1350 ºC. The temperature profile reveals the dynamic heat transfer from the outer shell to the sample's interior. As a result, the inner particles did not undergo the same thermal history as the outer particles most of the time, leading to an observable non-isothermal behavior caused by temperature gradients throughout the body.

Figure 4.6: Visualization of temperature profile inside the Al_2O_3 sample at 1050 and 1350 ºC for 30 to 180 s. The images correspond to a half-section view in the y-direction, with a thickness of 2 layers of particles.

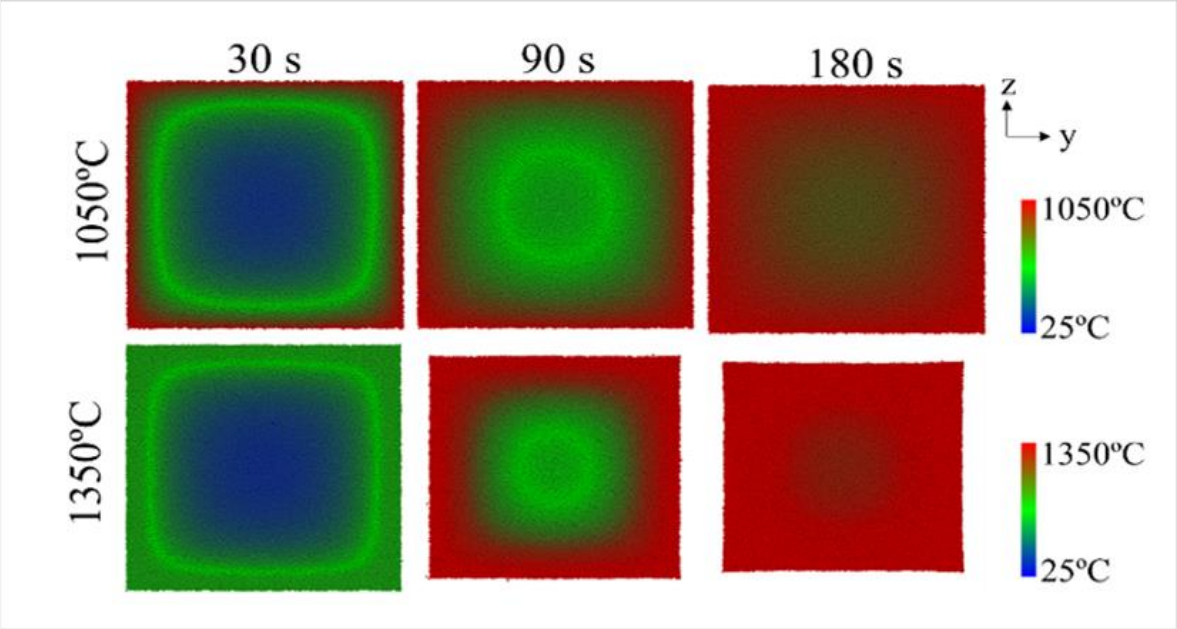

4.4 CONCLUSION

In this study, we successfully developed a discrete element method (DEM) model that effectively analyses and predicts phenomena occurring during fast sintering. Our model incorporates heat transfer concepts, transient temperature regimes, and sintering forces, enabling highly accurate simulations. Moreover, the model offers valuable insights into the densification process by revealing thermal-density gradients and the structural microkinetic evolution within the ceramic compact. The close alignment between the simulation and experimental results (R^2 = 0.99) underscores the reliability and precision of our approach. This successful validation using Al_2O_3 demonstrates the model's ability to confidently predict high heating rate sintering features. Overall, our developed DEM model holds great promise as a powerful tool for analyzing and predicting phenomena in fast sintering processes. Shedding light on the densification process and its underlying mechanisms opens new avenues for further exploration and optimization in this field.

CHAPTER 5 – FINAL REMARKS

5.1 CONCLUSIONS

A new model for the simulation of non-isothermal sintering was developed and applied to an Al2O3-based system within the DEM framework. The model integrates heat transfer concepts, transient temperature regime, and sintering, enabling the representation of fast sintering kinetics. It provided new insights into microscale features that contribute to the macro behavior of ceramics under rapid firing. The simulation results showed relevant details of the densification process, including thermal and density gradients and microkinetic evolution. Also, it well agreed with experimental data in the range analyzed.

5.2 SUGGESTIONS FOR FUTURE WORKS

For the continuation of this work, some suggestions are listed:

- Make an in-depth exploration of the model accuracy by rising:
  - sample properties - initial packing density, particle size and shape, packing size and shape;
  - sintering conditions - heating rate, sintering temperature;
  - material type – testing new materials besides alumina;
- Perform experiments to validate the simulations.

REFERENCES

ALVES, C. L. M. et al. Integrated process simulation of porcelain stoneware manufacturing using flowsheet simulation. **Cirp Journal of Manufacturing Science and Technology**, v. 33, p. 473–487, 2021.

ANDERSON, R. et al. Packed bed thermal energy storage: A simplified experimentally validated model. **Journal of Energy Storage**, v. 4, n. December, p. 14–23, 2015.

ASKARI, R.; HEJAZI, S. H.; SAHIMI, M. Effect of deformation on the thermal conductivity of granular porous media with rough grain surface. **Geophysical Research Letters**, v. 44, n. 16, p. 8285–8293, 2017.

BAE, S. I.; BAIK, S. Sintering and grain growth of ultrapure alumina. **Journal of Materials Science**, v. 28, n. 15, p. 4197–4204, 1993.

BAHRAMI, M.; CULHAM, J. R.; YOVANOVICH, M. M. Modeling thermal contact resistance: A scale analysis approach. **Journal of Heat Transfer**, v. 126, n. 6, p. 896–905, 2004.

BATCHELOR, G. K.; O'BRIEN, R. W. Thermal or Electrical Conduction Through a Granular Material. **Proc R Soc London Ser A**, v. 355, n. 1682, p. 313–333, 1977.

BERGMAN, T. L.; LAVINE, A. S. **Fundamentals of Heat and Mass Transfer**. 8th. ed. United States of America: John Wiley & Sons, Inc., 2017.

BERNARDO, E.; SCARINCI, G. Fast sinter crystallisation of waste glasses. **Advances in Applied Ceramics**, v. 107, n. 6, p. 344–349, 2008.

BESLER, R. et al. Sintering Simulation of Periodic Macro Porous Alumina. **Journal of the American Ceramic Society**, v. 98, n. 11, p. 3496–3502, 2015.

BESLER, R. et al. **Discrete element simulation of metal ceramic composite materials with varying metal content**. **Journal of the European Ceramic Society**, 2016.

BOUVARD, D.; MCMEEKING, R. M. Deformation of Interparticle Necks by Diffusion-Controlled Creep. **J. Am. Ceram. Soc.**, v. 79, n. 3, p. 666–672, 1996.

BURMAN, B. C.; CUNDALL, P. A.; STRACK, O. D. L. A discrete numerical model for granular assemblies. **Geotechnique**, v. 30, n. 3, p. 331–336, 1980.

C. L. MARTIN et al. Discrete element modeling of metallic powder sintering. **Scripta Materialia**, v. 55, n. 5, p. 425–428, 2006.

CAMM, L. Adventures in Fast Firing. **Ceramics & Refractories/Insulation**, 2017.

CHEN, L. et al. A DEM-based heat transfer model for the evaluation of effective thermal conductivity of packed beds filled with stagnant fluid: Thermal contact theory and numerical simulation. **International Journal of Heat and Mass Transfer**, v. 132, p. 331–346, 2019.

CHU, M.-Y. et al. Effect of heating rate on sintering and coarsening. **Refractories**, v. 74, n. 6, p. 1217–1225, 1991.

COBLE, R. L. Initial Sintering of Alumina and Hematite. **Journal of the American Ceramic Society**, v. 41, n. 2, p. 55–62, 1958.

COETZEE, C. J.; ELS, D. N. J. Calibration of granular material parameters for DEM modelling and numerical verification by blade-granular material interaction. **Journal of Terramechanics**, v. 46, p. 15–26, 2009.

DI RENZO, A.; PAOLO DI MAIO, F. An improved integral non-linear model for the contact of particles in distinct element simulations. **Chemical Engineering Science**, v. 60, n. 5, p. 1303–1312, 2005.

DONDI, M.; MARSIGLI, M.; VENTURI, I. Microstructure and mechanical properties of clay bricks: comparison between fast firing and traditional firing. **British Ceramic Transactions**, v. 98, n. 1, p. 12–18, 1999.

DOSTA, M. et al. Approximation of mechanical properties of sintered materials with discrete element method. **EPJ Web of Conferences**, v. 140, 2017.

DOSTA, M. et al. **DEM Analysis of Breakage Behavior of Bicomponent Agglomerates**. [s.l.] Springer International Publishing, 2019.

DOSTA, M. et al. **Influence of pores arrangement on stability of photonic structures during sintering**. **Journal of the European Ceramic Society**, 2020.

DOSTA, M.; SKORYCH, V. MUSEN: An open-source framework for GPU-accelerated DEM simulations. **SoftwareX**, v. 12, p. 100618, 2020.

DRANISHNYKOV, S.; DOSTA, M. Advanced approach for simulation results saving from discrete element method. **Advances in Engineering Software**, v. 136, n. July, p. 102694, 2019.

DUTRA, R. P. S. et al. Estudo comparativo da queima rápida com a queima tradicional nas propriedades de materiais cerâmicos de base argilosa. **Cerâmica**, v. 55, n. 333, p. 100–105, 2009.

European Power Metallurgy Association (EPMA).

FENG, Y. T.; HAN, K.; OWEN, D. R. J. Discrete thermal element modelling of heat conduction in particle systems: Pipe-network model and transient analysis. **Powder Technology**, v. 193, n. 3, p. 248–256, 2009.

Ferrous_Powder_Metallurgy. [s.d.].

FURLAN, K. P. **Estudo da sinterização e evolução microestrutural de misturas de Fe-MoS2**. Florianópolis: UFSC, 12 abr. 2013.

GANERIWALA, R.; ZOHDI, T. I. A coupled discrete element-finite difference model of selective laser sintering. **Granular Matter**, v. 18, n. 2, p. 1–15, 2016.

GARCÍA, D. E. et al. Fast firing of alumina. **Journal of the European Ceramic Society**, v. 15, n. 10, p. 935–938, 1995.

GARCÍA, D. E.; HOTZA, D.; JANSSEN, R. Building a sintering front through fast firing. **International Journal of Applied Ceramic Technology**, v. 8, n. 6, p. 1486–1493, 2011.

GARCÍA, D. E.; KLEIN, A. N.; HOTZA, D. Advanced ceramics with dense and fine-grained microstructures through fast firing. **Reviews on Advanced Materials Science**, v. 30, n. 3, p. 273–281, 2012.

GERMAN, R. M. Thermodynamics of sintering. In: FANG, Z. Z. (Ed.). **Sintering of Advanced Materials: Fundamentals and processes**. 1. ed. [s.l.] Woodhead Publishing Limited, 2010. p. 3–473.

GERMAN, R. M.; LATHROP, J. F. Simulation of spherical powder sintering by surface diffusion. **Journal of Materials Science**, v. 13, n. 5, p. 921–929, 1978.

GHORRA, G. J. Theory of Fast Firing. **Ceramic Engineering und Science Proceedings**, v. 115, p. 77–115, 2008.

GILLIA, O.; BOUVARD, D. Phenomenological analysis of densification kinetics during sintering: Application to WC-Co mixture. **Materials Science and Engineering A**, v. 279, n. 1–2, p. 185–191, 2000.

GÓMEZ, S. Y. et al. Nanocrystalline yttria-doped zirconia sintered by fast firing. **Materials Letters**, v. 166, p. 196–200, 2016.

GÓMEZ, S. Y.; HOTZA, D. Predicting powder densification during sintering. **Journal of the European Ceramic Society**, v. 38, n. 4, p. 1736–1741, 2018.

GRUPP, R. et al. Cooperative material transport during the early stage of sintering. **Nature Communications**, v. 2, n. 1, 2011.

HADDAD, H. et al. Numerical investigation of heat conduction in heterogeneous media with a discrete element method approach. **International**

Journal of Thermal Sciences, v. 164, n. February, 2021.

HADDAD, H.; GUESSASMA, M.; FORTIN, J. Heat transfer by conduction using DEM-FEM coupling method. **Computational Materials Science**, v. 81, p. 339–347, 2014.

HENRICH, B. et al. Simulations of the influence of rearrangement during sintering. **Acta Materialia**, v. 55, n. 2, p. 753–762, 2007.

HOGUE, M. D. et al. Calculating the trajectories of triboelectrically charged particles using Discrete Element Modeling (DEM). **Journal of Electrostatics**, v. 66, n. 1–2, p. 32–38, 2008.

IACOBELLIS, V.; RADHI, A.; BEHDINAN, K. Discrete element model for ZrB2-SiC ceramic composite sintering. **Composite Structures**, v. 229, n. August 2018, p. 111373, 2019.

JAUFFRÈS, D. et al. **Simulation of the toughness of partially sintered ceramics with realistic microstructures**. **Acta Materialia**, 2012.

JI, W. et al. Ultra-fast firing: Effect of heating rate on sintering of 3YSZ, with and without an electric field. **Journal of the European Ceramic Society**, v. 37, n. 6, p. 2547–2551, jun. 2017.

KANG, S.-J. L. Liquid phase sintering. In: **Sintering of Advanced Materials**. New York, NY: Sringer Science & Business Media, 2010. p. 110–129.

KIANI-OSHTORJANI, M.; JALALI, P. Thermal discrete element method for transient heat conduction in granular packing under compressive forces. **International Journal of Heat and Mass Transfer**, v. 145, p. 118753, 2019.

KOZHAR, S. et al. DEM simulations of amorphous irregular shaped micrometer-sized titania agglomerates at compression. **Advanced Powder Technology**, v. 26, n. 3, p. 767–777, 2015.

L.KANG, S.-J. **Sintering Processes**. [s.l.] Elsevier Ltd, 2005.

L.WANG; SUN., J. Numerical simulation of radiation heat transfer characteristics in a cylindrical fluidized bed. **Heat and Mass Transfer/Waerme- und Stoffuebertragung**, v. 56, n. 7, p. 2025–2034, 2020.

LIANG, Y.; LI, X. A new model for heat transfer through the contact network of randomly packed granular material. **Applied Thermal Engineering**, 2014.

LICHTNER, A. et al. **Anisotropic sintering behavior of freeze-cast ceramics by optical dilatometry and discrete-element simulations**. **Acta Materialia**, 2018.

LIN, F. J. T.; DE JONGHE, L. C.; RAHAMAN, M. N. Initial coarsening and microstructural evolution of fast-fired and MgO-doped Al2O3. **Journal of the American Ceramic Society**, v. 80, n. 11, p. 2891–2896, 1997.

MAHI, F. T.; KWON, O.-H. Liquid Phase Sintering: Ceramics. In: **Reference Module in Materials Science and Materials Engineering**. [s.l.] Elsevier, 2016.

MARTIN, C. L. et al. Evolution of defects during sintering: Discrete element simulations. **Journal of the American Ceramic Society**, v. 92, n. 7, p. 1435–1441, 2009.

MARTIN, C. L. et al. Sintered ceramics with controlled microstructures: Numerical investigations with the Discrete Element Method. **Journal of the Ceramic Society of Japan**, v. 124, n. 4, p. 340–345, 2016a.

MARTIN, C. L.; BORDIA, R. K. The effect of a substrate on the sintering of constrained films. **Acta Materialia**, v. 57, n. 2, p. 549–558, 2009.

MARTIN, S. et al. Simulation of sintering using a Non Smooth Discrete Element Method. Application to the study of rearrangement. **Computational Materials Science**, v. 84, p. 31–39, 2014.

MARTIN, S. et al. Validation of DEM modeling of sintering using an in situ X-ray microtomography analysis of the sintering of NaCl powder. **Computational Particle Mechanics**, v. 3, n. 4, p. 525–532, 2016b.

MINDLIN, R. D.; DERESIEWICZ, H. Elastic spheres in contact under varying oblique force. **J. Appl. Mech**, v. Trans. ASM, n. 20, p. 327–344, 1953.

MORI, K. Finite element simulation of powder forming and sintering. **Computer Methods in Applied Mechanics and Engineering**, v. 195, n. 48–49, p. 6737–6749, 2006.

MOSCARDINI, M. et al. Discrete element method for e ff ective thermal conductivity of packed pebbles accounting for the Smoluchowski e ff ect. **Fusion Engineering and Design**, v. 127, n. June 2017, p. 192–201, 2018.

MOSKAL, G.; MIKUŚKIEWICZ, M.; JASIK, A. Thermal diffusivity measurement of ceramic materials used in spraying of TBC systems: The influence of materials' morphology and (re)manufacturing processes. **Journal of Thermal Analysis and Calorimetry**, v. 138, n. 6, p. 4261–4269, 2019.

NOSEWICZ, S. et al. Viscoelastic discrete element model of powder sintering. **Powder Technology**, v. 246, p. 157–168, 2013.

NOSEWICZ, S. et al. Application of the Hertz formulation in the discrete

element model of pressure-assisted sintering. **Granular Matter**, v. 19, n. 1, p. 1–8, 2017.

NOSEWICZ, S.; ROJEK, J.; CHMIELEWSKI, M. Discrete element framework for determination of sintering and postsintering residual stresses of particle reinforced composites. **Materials**, v. 13, n. 18, p. 1–21, 2020.

O'SULLIVAN, C.; BRAY, J. D. Selecting a suitable time step for discrete element simulations that use the central difference time integration scheme. **Engineering Computations (Swansea, Wales)**, v. 21, n. 2–4, p. 278–303, 2004.

PARHAMI, F. et al. A model for the sintering and coarsening of rows of spherical particles. **Mechanics of Materials**, v. 31, n. 1, p. 43–61, 1999.

PARHAMI, F.; MCMEEKING, R. M. A network model for initial stage sintering. **Mechanics of Materials**, v. 27, n. 2, p. 111–124, 1998.

PENG, Z.; DOROODCHI, E.; MOGHTADERI, B. Heat transfer modelling in Discrete Element Method (DEM)-based simulations of thermal processes: Theory and model development. **Progress in Energy and Combustion Science**, v. 79, 2020.

PINTO, M. F.; SOUSA, S. J. G.; HOLANDA, J. N. F. Efeito do ciclo de queima sobre as propriedades tecnológicas de uma massa cerâmica vermelha para revestimento poroso. **Cerâmica**, v. 51, n. 319, p. 225–229, 2005.

POSSAMAI, T. S. et al. Numerical simulation of the fast firing of alumina in a box furnace. **Journal of the American Ceramic Society**, v. 95, n. 12, p. 3750–3757, 2012.

QING, Z. et al. Crystallization kinetics, sintering, microstructure, and properties of low temperature co-fired magnesium aluminum silicate glass-ceramic. **Journal of Non-Crystalline Solids**, v. 486, p. 14–18, abr. 2018.

RAETHER, F.; SCHULZE HORN, P. Investigation of sintering mechanisms of alumina using kinetic field and master sintering diagrams. **Journal of the European Ceramic Society**, v. 29, n. 11, p. 2225–2234, 2009.

RAHAMAN, M. N. **Ceramic Processing and Sintering**. 2nd. ed. Boca Raton: CRC Press, 2003.

RAHAMAN, M. N. **Sintering of Ceramics**. 1st. ed. Boca Raton: CRC Press., 2007.

RASP, T. et al. **Cracking and shape deformation of cylindrical cavities during constrained sintering**. **Journal of the European Ceramic Society**, 2017.

RASP, T.; KRAFT, T.; RIEDEL, H. Discrete element study on the influence of

initial coordination numbers on sintering behaviour. **Scripta Materialia**, v. 69, n. 11–12, p. 805–808, 2013.

REED, J. S. **Principles of ceramic processing**. 2nd. ed. New York: Willey, 1995.

RIERA, J. D.; MIGUEL, L. F. F.; ITURRIOZ, I. Evaluation of the discrete element method (DEM) and of the experimental evidence on concrete behaviour under static 3D compression. **Fatigue & Fracture of Engineering Materials & Structures**, v. 39, n. 11, p. 1366–1378, 2016.

ROCK, A. D.; ZHANG, R.; DAVID WILKINSON, P. E. **Velocity Variations in Cross-Hole Sonic Logging Surveys Causes and Impacts in Drilled Shafts**. [s.l: s.n.].

ROUSSEAU, P. G. et al. Separate effects tests to determine the effective thermal conductivity in the PBMR HTTU test facility. **Nuclear Engineering and Design**, v. 271, p. 444–458, 2014.

SANGRÓS, C.; SCHILDE, C.; KWADE, A. Effect of Microstructure on Thermal Conduction within Lithium-Ion Battery Electrodes using Discrete Element Method Simulations. **Energy Technology**, v. 4, n. 12, p. 1611–1619, 2016.

SEAL, A. et al. Fast firing of lead zirconate titanate ceramics at low temperature. **Materials Chemistry and Physics**, v. 97, n. 1, p. 14–18, maio 2006.

SINGH, K. K.; SUBRAHMANYAM. Fast firing of ceramics—a review. **Transactions of the Indian Ceramic Society**, v. 35, n. 1, p. 26–30, 1976.

SOMTON, K. et al. Shrinkage and properties of die pressed alumina produced from different granule sources. **AIP Conference Proceedings**, v. 2279, n. October, 2020.

TATAMI, J. et al. Control of shrinkage during sintering of alumina ceramics based on Master Sintering Curve theory. **Key Engineering Materials**, v. 317–318, p. 11–14, 2006.

TEIXEIRA, M. H. P. et al. High heating rate sintering and microstructural evolution assessment using the discrete element method. **Open Ceramics**, v. 8, p. 100182, 2021.

TERREROS, I.; IORDANOFF, I.; CHARLES, J. L. Simulation of continuum heat conduction using DEM domains. **Computational Materials Science**, v. 69, p. 46–52, 2013.

TSUJI, Y.; TANAKA, T.; ISHIDA, T. Lagrangian numerical simulation of plug

flow of cohesionless particles in a horizontal pipe. **Powder Technology**, v. 71, n. 3, p. 239–250, 1992.

VARGAS, W. L.; MCCARTHY, J. J. Conductivity of granular media with stagnant interstitial fluids via thermal particle dynamics simulation. **International Journal of Heat and Mass Transfer**, v. 45, n. 24, p. 4847–4856, 2002.

WANG, D. et al. Densification mechanism of the ultra-fast sintering dense alumina. **AIP Advances**, v. 10, n. 2, 2020.

WANG, X.-H.; CHEN, I.-W. Sintering dense nanocrystalline ceramics without final-stage grain growth. **Nature**, v. 404, n. 9 March, p. 168–171, 2000.

WEBER, M. et al. Simulation-based investigation of core-shell agglomerates: Influence of spatial heterogeneity in particle sizes on breakage characteristics. **Computational Materials Science**, v. 137, p. 100–106, 2017.

WONISCH, A. et al. Stress-induced anisotropy of sintering alumina: Discrete element modelling and experiments. **Acta Materialia**, v. 55, n. 15, p. 5187–5199, 2007.

WU, H. et al. Numerical simulation of heat transfer in packed pebble beds: CFD-DEM coupled with particle thermal radiation. **International Journal of Heat and Mass Transfer**, v. 110, p. 393–405, 2017.

ZHANG, J. et al. The nature of grain boundaries in alumina fabricated by fast sintering. **Scripta Materialia**, v. 62, n. 9, p. 658–661, 2010.

ZHOU, Q.; ZHANG, H. W.; ZHENG, Y. G. A homogenization technique for heat transfer in periodic granular materials. **Advanced Powder Technology**, v. 23, n. 1, p. 104–114, 2012.

APPENDIX

COMPLEMENTARY EQUATIONS AND TABLES OF CHAPTER 3

$$\delta_n = R_i + R_j - |\vec{X}_i - \vec{X}_j| \quad \text{(A.1)}$$

$$K_n = 2\,E^*\sqrt{R^*\,\delta_n^{HM}} \quad \text{(A.2)}$$

$$B_n = 1.8257\,\mu\sqrt{K_n\,m^*} \quad \text{(A.3)}$$

$$K_t = 8\,G^*\sqrt{R^*\,\delta_n^{HM}} \quad \text{(A.4)}$$

$$\Delta\delta_t = v_{rel,t}\,\Delta t \quad \text{(A.5)}$$

$$B_t = 1.8257\,\mu\sqrt{K_t\,m^*} \quad \text{(A.6)}$$

$$\mu = \frac{-\ln^2 e}{\sqrt{\pi^2 + \ln^2 e}} \quad \text{(A.7)}$$

$$m^* = \frac{m_i\,m_j}{m_i + m_j} \quad \text{(A.8)}$$

$$R^* = \frac{R_i\,R_j}{R_i + R_j} \quad \text{(A.9)}$$

$$E^* = \left(\frac{1-\nu_i^2}{E_i} + \frac{1-\nu_j^2}{E_j}\right)^{-1} \quad \text{(A.10)}$$

$$G^* = \left(\frac{2-\nu_i}{G_i} + \frac{2-\nu_j}{G_j}\right)^{-1} \quad \text{(A.11)}$$

where E^*, R^*, m^*, and G^* are the equivalent young's modulus, radius, mass, and shear modulus of the two contacting bodies, e is the restitution coefficient, and ν is Poisson's ratio.

Table A.1. Summary of TMS model parameters.

Parameters	Symbol	Unit	Value
Convective heat transfer	h_c	W/m^2·K	5
Factor of mass scaling	S_{m_p}	-	$1.8 \cdot 10^{19}$
Factor of size scaling for length dependency	S_ℓ	-	$1.21 \cdot 10^{-6}$
Factor of size scaling for surface dependency	S_a	-	$1.1 \cdot 10^{-3}$
Heating rate	Ř	ºC/s	0.17-Instant.
Initial temperature	T_0	K	298.15 - 373.15
Initial temperature of particles	T_o	K	298
Inner temperature of furnace	T_{env}	K	1323.15 - 1623.15
Maximum average normal overlap	λ_{max}	-	0.05
Minimum average normal overlap	λ_{min}	-	0.03
Minimum temperature for sintering	T_{min}^{sint}	K	1373.15
Poisson's ratio	ν	-	0.23
Restitution coefficient	e	-	0.1
Simulation time step	Δt	s	0.001
Sintering model parameter	α	-	4
Sintering model parameter	β	-	4.5
Slip parameter	η	-	0.01
Stefan-Boltzmann constant	σ	W/m^2·K^4	$5.67 \cdot 10^{-8}$
Stop criterion	$\max r_c/R$	-	0.8
Surface emissivity	ε	-	0.8
Thermal conduction resistivity factor	f_{res}	-	0.18
Treatment temperature	T	K	1523.15 - 1623.15